Towards a complete Himalayan hydrological budget: The spatiotemporal distribution of

snowmelt and rainfall and their impact on river discharge

Bodo Bookhagen[1], Douglas W. Burbank[2]

1Geography Department, UC Santa Barbara, Santa Barbara, CA 93106, USA

2Institute for Crustal Studies, UC Santa Barbara, Santa Barbara, CA 93106, USA

Abstract

The hydrological budget of Himalayan rivers is dominated by monsoonal rainfall and snowmelt, but their relative impact is not well established. Current knowledge of rainfall and snow-cover distribution is unreliable because this remote region lacks a dense gauge network. Here, we use a combination of remotely-sensed climate parameters that have been both calibrated and validated to characterize the spatiotemporal distribution of rainfall, snowfall, and evapotranspiration in order to quantify their relative contribution to mean river discharge. Rainfall amounts are calculated from explicitly calibrated, orbital, high-resolution (~5x5 km) TRMM (Tropical Rainfall Measurement Mission) data, and snow-water equivalents are computed from a snowmelt model based on satellite-derived snow cover, surface temperature, and solar radiation. Despite complex hydrological interactions, we are able to hindcast river flows within 5% of their monthly measured values from a river-gauge network with daily measurements spanning the entire Himalaya. Our data allow us to identify five key aspects of the spatiotemporal precipitation pattern. First, we observe a strong decoupling between the rainfall on the Himalayan foreland versus that in the mountains: a pronounced 6-fold, east-west rainfall gradient in the Ganges plains exists only at elevations < 500 m asl. Mountainous regions (500 to 5000 m asl) receive nearly equal rainfall amounts along strike, such that the overall rainfall

24 amounts flowing into the orogen remain remarkably uniform during the summer monsoon along

25 much of the Himalaya. Second, within the mountains, progressive rainfall loss correlates with

26 topographic relief on southward-facing slopes, thereby suggesting that relief is an important

27 predictor of orographic-rainfall efficiency. Third, whereas the Indian summer monsoon is

28 responsible for more than 80% of annual rainfall in the central Himalaya and Tibetan Plateau, the

29 eastern and western syntaxes (i.e., the Himalayan part of the Tsangpo and Indus catchments,

30 respectively) receive only ~50% of their annual rainfall during the summer season. Fourth, the

31 most intense rainfall events occur in the western Himalaya and to the south of the Shillong

32 Plateau where lightning rates are among the highest in the world and rainfall intensities exceed

33 50 mm/hr. Fifth, snowmelt contributions to discharge differ widely along the range. As a fraction

34 of the total annual discharge, snowmelt constitutes up to 50% in the far western (Indus area)

35 catchments, ~25% in far eastern (Tsangpo) catchments, and <20% elsewhere. Despite these

36 along-strike variations, snowmelt in the pre- and early-monsoon season (April to June) is

37 significant and important in all catchments, although most pronounced in the western

38 catchments. Thus, changes in the timing or amount of snowmelt due to increasing temperatures

39 or decreasing winter precipitation may have far-reaching societal consequences. These new data

40 on precipitation and runoff set the stage for far more detailed investigations than have previously

41 been possible of climate-erosion interactions in the Himalaya.

42 **1. Introduction**

43   The Himalaya and adjacent Tibetan Plateau are the source of several major Asian

44 rivers supporting a large, diverse ecosystem and a population of more than 1 billion people [*Ives*

45 *and Messerli*, 1989]. Large rivers such as the Indus, Sutlej, Ganges, Arun, and

46 Brahmaputra/Tsangpo draining the southern Tibetan Plateau and the Himalaya (Figure 1) are

2

47   essential for agriculture and energy generation and are the pathways for sediments leaving the

48   orogen. The precipitation in the upstream and high-elevation parts of these basins falls as snow,

49   causing a natural delay in the river discharge. Snow cover dynamics in the High Himalaya and

50   on the Tibetan Plateau, therefore, influence the water availability downstream in the major river

51   basins of Asia, specifically in the spring at the onset of the growing season, but also in the fall

52   after the monsoon season [*Barnett et al.*, 2005; *Guntner et al.*, 2007; *Immerzeel et al.*, 2009;

53   *Kundzewicz et al.*, 2007; *Lemke et al.*, 2007; *Viviroli et al.*, 2007*; Singh and Kumar, 1997*]. In

54   the Himalayan foreland and at low to moderate elevations, precipitation is dominated by rainfall

55   during the Indian summer monsoon season [*Anders et al.*, 2006; *Bookhagen et al.*, 2005a;

56   *Bookhagen and Burbank*, 2006]. Along the southern Himalayan front, a strong south-to-north

57   rainfall gradient exists with wet, southern areas near the Ganges Plains and arid, northern regions

58   toward the Tibetan Plateau [*Burbank et al., 2003*].

59   In this paper we explore the relative spatiotemporal influence of snowmelt, rainfall and

60   evapotranspiration on river flow. We focus our analyses on 27 major catchments draining the

61   southern Himalayan front, stretching from the Indus in the west to the Tsangpo / Brahmaputra

62   River in the east. We use high-resolution, calibrated, remotely-sensed rainfall values combined

63   with a simple, but robust snowmelt model based on satellite-derived snow cover, air temperature,

64   and solar radiation to quantify relative discharge contributions. We validate our results with daily

65   river-gauge stations spanning the entire Himalayan front.

66   Overall, our analysis reveals five important attributes of Himalayan precipitation and

67   runoff. First, we have improved previous remotely-sensed TRMM (Tropical Rainfall

68   Measurement Mission) rainfall estimates [*Bookhagen and Burbank*, 2006] by using a dense

69   network of more than 1700 ground-control stations as calibration locations, by accounting more

70   completely for satellite orbital geometry, by developing an improved interpolation algorithm for

71   the orbital data, and by including spatial error estimates for the data. Second, we demonstrate the

72   importance of high-spatial resolution rainfall data to develop more robust rainfall-topography

73   relations, and we demonstrate the significance of seasonal rainfall variations along strike of the

74   Himalaya and their implications for the hydrological budget. Third, we have processed remotely-

75   sensed lightning data from the TRMM-LIS (Lightning Image Sensor) satellite to identify regions

76   of heavy convective activity that results in violent cloudbursts. We use these data in combination

77   with rainfall intensity measurements to outline regions where high-magnitude rainfall events are

78   more common during the past decade. Fourth, in order to describe the hydrological budget of the

79   Himalaya, we create a satellite-based snowmelt model that uses MODIS (Moderate Resolution

80   Imaging Spectroradiometer) snow-cover data, land-surface temperatures, and solar radiation. We

81   limit our analysis to the mountainous regions where evapotranspiration generally has a low

82   impact on overall catchment hydrology (<10%). Nonetheless, we directly estimate

83   evapotranspiration amounts from a MODIS product. Finally, river-gauge data indicate that, using

84   our combined rainfall, snowmelt, and evapotranspiration model, we can predict average monthly

85   discharge within <5% of their measured amounts. These predictions gain importance not only for

86   understanding the hydrological budget, snowmelt magnitude, and timing of discharge, but also

87   for studies using discharge as a predictor for fluvial erosion or as a key input for landscape

88   evolution models.

89   **2.   Methods and Datasets**

90   **2.1 Topographic data**

91   We used the Shuttle Radar Topographic Mission (SRTM) Version 2 topographic data

92   with a 90-m grid-cell size for our analysis [*Farr et al.*, 2007]. After filling holes in the SRTM

4

93   data [See the supplementary data for a more complete description of data processing], the entire,

94   combined 90-m dataset was hydrologically corrected using the method described by Garbrecht

95   and Martz [1997].

96   **2.2 TRMM (Tropical Rainfall Measurement Mission) rainfall**

97   We used raw, orbital satellite data from the Tropical Rainfall Measurement Mission

98   (TRMM) to estimate rainfall amounts [*Kummerow et al.*, 1998; *Kummerow et al.*, 2000]. The

99   TRMM product 2B31 provides rainfall estimates on a ~4x6 km^2 pixel size between 36°N and

100   36°S (TRMM product 2B31, algorithm V6, more information available at:

101   http://disc.sci.gsfc.nasa.gov/precipitation/documentation/TRMM_README/TRMM_2B31_read

102   me.shtml). The TRMM 2B31 data product is a combined rainfall profile product from the

103   Precipitation Radar (PR) and TRMM Microwave Imager (TMI). We processed these data for 10

104   consecutive years from 1998 to 2007 with a total of 57,718 orbits (~16 each day) and

105   interpolated the orbital data onto an equally-spaced 5x5 km^2 grid. In August 2001, the orbital

106   boost maneuver to extend the lifetime of the TRMM platform resulted in a change of the

107   horizontal footprint resolution to ~5.0 km. [See the supplementary data for a more complete

108   description of data processing and error estimations.] For Himalayan-Tibetan areas lying north of

109   36°N, we used the TRMM product 3B42 that includes data from the Special Sensor

110   Microwave/Imager, the Advanced Microwave Scanning Radiometer, and the Advanced

111   Microwave Sounding Unit to estimate precipitation at a spatial scale of 0.25x0.25° (~30x30 km)

112   [*Huffman, et al. 2007*].

113   The instantaneous rainfall amounts (mm/hr) were converted (or calibrated) to mean

114   seasonal or annual rainfall (m/yr) with daily and monthly, ground-based rainfall measurements

115   from the greater Himalaya realm (n = 1741, see Figure 1B for location and Figures 2 and DR3

116 for calibrations as well as the Data Repository for more information) [*Barros et al.*, 2000;

117 *Bookhagen and Burbank*, 2006; *GDCNV1*, 2002]. Generally, the data reveal robust and

118 consistent results, even though the stations span >10° in latitude, >30° in longitude, and an

119 elevation range from sea level to 4.5 km asl (Figures 1B and 2 and DR2). Most of the heavy

120 rainfall occurs below 4 km [*Barros et al.*, 2000; *Bookhagen and Burbank*, 2006; *Parthasarathy*

121 *et al.*, 1992] and almost none above 6 km [*Harper and Humphrey*, 2003]. We used the rainfall

122 datasets to calculate the river flow from the upstream drainage area using the 90-m flow routing

123 grid derived from the patched topographic data [*Tarboton et al.*, 1991]. We have routed the flow

124 both monthly and annually.

125   Our rainfall calibration parameters that convert rainfall intensities to mean annual

126 rainfall are very similar to those from a similar study in the Andes of South America with nearly

127 2000 gauge stations [*Bookhagen and Strecker*, 2008]. In general, the remotely-sensed rainfall

128 data correlate well with the ground-control stations; even high annual-rainfall amounts above 5

129 m/yr are accurately depicted (Figures 2 and DR2). We have performed several calibration

130 routines in which we included only rain-gauge stations from below 0.5 km asl (n = 1398) or from

131 above 0.5 km (n = 343) and their respective conversion factors differ only by ~6%. In this study,

132 we rely on conversions factors between instantaneous and seasonal or annual rainfall (mm/hr to

133 m/yr) based on all station data (Figure 2). This corroborates our earlier findings from the

134 Himalaya indicating that, despite non-continuous TRMM-rainfall data series, relative values

135 represent a valid rainfall distribution [*Bookhagen and Burbank*, 2006].

136   We summarize here the additional steps we took to improve our previous rainfall

137 estimates [*Bookhagen and Burbank*, 2006]: (1) bilinear interpolation of every orbit of the TRMM

138 2B31 RR-Surf product onto an equally spaced grid to homogenize the data (this includes a

139 correction for pre- and post-boost orbits), (2) calibration with 1741 ground-control stations to

140 create a robust calibration factor for conversion from instantaneous rainfall rates measured in

141 mm/hr to mean annual or seasonal rainfall amounts (m/yr), and (3) inclusion of error estimations

142 for satellite and rain-gauge measurements to provide precision boundaries.

143   In a separate calibration effort to convert instantaneous rainfall amounts (mm/hr) to

144 mean seasonal or mean annual amounts (m/yr), we have analyzed data from the 46-day TRMM

145 cycle. This conversion method was previously used by researchers for estimating Himalayan

146 rainfall using a Precipitation Radar product (TRMM 2A25) [*Anders et al.*, 2006; *Finnegan et al.*,

147 2005]. Except for being in the same position at the same time at the start of each cycle, the

148 satellite's orbit samples each location at different times of day during a cycle [*Kummerow et al.*,

149 1998]. It has been argued that by dividing each year into approximately eight 46-day periods, an

150 even sampling of the diurnal cycle is produced [*Anders et al.*, 2006; *Kummerow et al.*, 1998].

151 The average rain rate within each period is then multiplied by its length to estimate the rainfall

152 amounts [*Anders et al.*, 2006; *Kummerow et al.*, 1998]. The sum of eight periods results in the

153 mean annual rainfall. We compare this conversion scheme to the rain-gauge data and find that,

154 although it yields a strong correlation ($r^2 = 0.87$), it overpredicts observed absolute rainfall by

155 ~45% (Figure DR3). Furthermore, this simplified calibration scheme with 8 values per year

156 results in mean annual rainfall rates only and does not allow analysis at a higher temporal

157 (seasonal) resolution.

158 **2.3 TRMM Lightning Image Sensor (LIS)**

159   We used the Lightning Imaging Sensor (LIS) onboard the TRMM satellite to

160 determine the distribution and variability of lightning (cloud-to-cloud, intra-cloud, and cloud-to-

161 ground lightning) at the same time as rainfall measurements were made. [See the supplementary

162   data for a more complete description.] The LIS represents a significant advance over any

163   previous satellite-borne lightning detector. LIS observations can be readily associated with the

164   thunderstorms that produced them. The detection of even a single lightning discharge is

165   significant and provides important information bearing on storm location, rainfall estimates,

166   storm height, the presence of ice, and lightning frequency [e.g., *Petersen and Rutledge*, 2001].

167   **2.4 Evapotranspiration**

168   We have used a global evapotranspiration algorithm based on MODIS and global

169   meteorology data described in *Cleugh et al.* [2007], *Mu et al.* [2007] and *Sun et al.* [2007]. This

170   algorithm is based on the Penman-Monteith method and considers both the surface energy

171   partitioning process and environmental constraints on evapotranspiration [*Cleugh et al.*, 2007;

172   *Monteith*, 1964]. The improved algorithm developed by *Mu et al.* [2007] was evaluated with 19

173   AmeriFlux eddy covariance flux towers and shows a strong (r^2 = 0.76) correlation with the field

174   data. [See the supplementary data for a more complete description of data processing.] For the

175   western Himalaya, we have compared basin-average evapotranspiration estimates derived from

176   the MODIS algorithm with in-situ field measurements [*Singh et al.*, 1997] and find good

177   agreement.

178   **2.5 Snow-cover area, surface temperature, and solar radiation**

179   We have used data from the Moderate Resolution Imaging Spectroradiometer

180   (MODIS) to quantify snow cover (MOD10) and surface temperature (MOD11) [*Hall et al.*,

181   2002; *Hall and Casey*, 2003; *Wan et al., 2004; Wan and Dozier*, 1996; *Wan et al.*, 2002]. [See

182   the supplementary data for a more complete description of data processing.] The MOD10C2

183   product yields pixel values indicating the percentage of snow cover within a 0.05x0.05° (~6x6

184   km) grid cell over an 8-day period. With these values, we calculate mean monthly snow-cover

185   areas from 2000 to 2008.

186   To estimate land surface temperature, we have used the MODIS land surface

187   temperature observations (MOD11C2) that are collected at the same spatial scale as the snow-

188   cover data [*Wan et al.*, 2004]. These temperature data are then used to calculate the days with a

189   mean temperature above freezing.

190   We have calculated mean monthly solar radiation for each 1x1 km grid cell from our

191   DEM using an approach described in *Kumar et al.* [1997]. This method calculates the clear-sky

192   radiation corrected for the incident angle, plus both diffuse and reflected radiation. This total

193   radiation correction can be significant, because the steep terrain results in considerable self-

194   shading. Insolation depends on time of year and day, latitude, elevation, slope, and aspect. We

195   first calculate hourly solar radiation and then derive a mean monthly amount from this.

196   **2.6 Parameterization of the snowmelt model**

197   In general, runoff modeling is concerned with the transformation of incoming

198   precipitation to outgoing streamflow, while taking into account losses to the atmosphere,

199   temporary storage, and both lag and attenuation as water is routed by fast and slow pathways

200   above and below the ground. When precipitation falls as snow, rather than rain, a snowpack

201   accumulates until warmer weather allows melting. Melt water is routed by the same pathways as

202   rainfall, so most snowmelt models are rainfall-runoff models with extra routines added to store

203   and subsequently melt precipitation that falls as snow. Several related semi-empirical approaches

204   quantify lag times, transient storage of moisture in mountainous catchments, and conversion of

205   snow into snow-water equivalents, including the Soil and Water Assessment Tool (SWAT)

206   model [e.g., *Arnold and Fohrer*, 2005], the degree-day method [e.g., *Hock*, 2003; *Linsley*, 1943;

207   *Rango and Martinec*, 1995], the snowmelt-runoff model [e.g., *Brubaker et al.*, 1996], and snow

208   accumulation and ablation models using the physics of snow-cover energy exchange [e.g.,

209   *Anderson*, 1973; *Franz et al.*, 2008]. Despite some of the models' simplicity, they generally

210   perform well when predicting discharges in snow-covered mountainous terrain [e.g., *Ferguson*,

211   1999; *Hock*, 2003; *Immerzeel et al.*, 2009; *Rango and Martinec*, 1995].

212   We have employed a modified snowmelt runoff model (SRM) that uses solar radiation

213   and temperature to convert snow-covered areas into a melt-water runoff component. The

214   radiation term is important in low latitude, high-elevation mountain belts because high solar

215   radiation causes melt-water generation at temperatures below the freezing level. The snowmelt

216   S_{melt} is calculated using the following relation:

217        $$S_{melt} = m_Q * R + a_r * T \qquad \text{(Equation 1)}$$

218   where m_Q is the physical constant converting energy to water mass or depth (0.026 cm W^{-1} m^2

219   day^{-1}), R is the incident solar radiation, a_r a restricted degree-day factor (cm °C^{-1} day^{-1}), and T

220   the mean daily temperature (°C). We have followed Rango and Martinec [1995] and modified

221   the equation (i) to reflect the number of degree days above 0 °C taken from the MODIS land

222   surface temperature data and (ii) to include the per-pixel snow-covered area derived from the

223   MODIS Snow Cover data. Our approach has then been applied to 1x1 km pixels, a spatial-

224   resolution compromise between data availability and steep climatic gradients in the Himalaya.

225   We have limited our analysis to mean-monthly estimates that allow us to identify seasonal

226   patterns on a large, regional scale. In summary, we have used the following parameterization to

227   estimate snowmelt volume (S_V) and iteratively applied it to each pixel with the corresponding

228   fractional snow cover (A_s), solar radiation (R), and days above freezing (T_d).

229        $$S_V = A_s \, (m_Q * R + a_r * T_d) \qquad \text{(Equation 2)}$$

230   For each month, we have used a different restricted degree-day factor (a_r), varying

231   between 0.2 and 0.8 with higher values in the summer season. These values have been used for

232   similar modeling efforts in mountainous terrain [*Martinec et al.*, 2007; *Rango and Martinec*,

233   1995] and are intended to capture the observed seasonal variability, i.e., more melting during

234   summer months for the same mean temperature mostly due to snow-density changes. Our

235   approach differs from previous approaches in that we explicitly model each pixel separately

236   instead of dividing the catchment into regions with similar climatic characteristics [e.g.,

237   *Immerzeel et al.*, 2009; *Martinec et al.*, 2007]. The satellite-derived temperature, snow cover, and

238   solar-radiation data allow us to generate spatially continuous measurements without the need to

239   interpolate from a sparse station network.

240   In a final step, we combine our mean-monthly TRMM rainfall data with the snowmelt

241   model and evapotranspiration data to estimate discharges. We assume a combined rainfall and

242   snowfall-runoff coefficient of 0.7, based on previous studies in the Himalaya [*e.g., Rao et al.,*

243   *1996;Hasnain, 1999; Singh et al., 1997*]. We validate our modeled discharge data with a daily

244   river-gauging network spanning the entire Himalaya (see Figure 1A for location). In general, our

245   monthly predicted discharges match measurements within 10% (Figure 3, DR4). Importantly,

246   runoff derived only from rainfall amounts underpredicts discharge on average by ~40%.

247   **3.   Study area and climatic background**

248   Generally, two independent climatic regimes dominate the Himalaya domain: the

249   monsoon system and the westerlies. The monsoon system is generally divided into the East

250   Asian and Indian monsoon systems; these systems strongly interact and influence each other. For

251   a more complete description of the complex relationships between vertically integrated

252   atmospheric temperature, pressure, and rainfall content, we refer to *Webster* [1987], *Webster et*

253 *al.* [1998], *Gadgil et al.* [2003], and *Wang* [2006] and to *Ding and Chan* [2005] for an overview

254 of the East Asian monsoon. However, in order to understand the spatiotemporal precipitation

255 variations in the Himalaya domain, especially the importance of its seasonal impacts, a basic

256 knowledge of the two general circulation patterns is essential.

257   The height and extent of the Tibetan Plateau and High Himalaya impose a significant

258 barrier to atmospheric circulation patterns. For the past decades, several authors have argued that

259 the strength of the South Asian monsoon is related to the high solar insolation on the Tibetan

260 Plateau during the summer time [*Barros et al.*, 2004; *Bookhagen et al.*, 2005b; *Flohn*, 1957;

261 *Gadgil et al.*, 2003; *Webster*, 1987]. In their models, during summer, the highly elevated, solar-

262 heated Tibetan Plateau develops a near surface, low-pressure cell, causing the atmosphere to re-

263 arrange its circulation patterns, which ultimately leads to strong near-surface winds in the region

264 surrounding the plateau [the word monsoon is derived from the Arabic word for season and is

265 used to delineate the wind-direction reversal during this time]. However, other previous and

266 recent studies argue that the high orographic barrier produces a strong monsoon by insulating

267 warm, moist air over continental India from the cold and dry northern latitudes [e.g., *Boos and*

268 *Kuang*, 2010]. One of the main driving forces of the monsoon at its onset stage is the

269 temperature gradient between the warm land and cooler ocean. Latent-heat release via

270 condensation over the Indian continent contributes significantly to maintain this temperate

271 gradient during the active part of the monsoon season [e.g., *Fasullo and Webster*, 2003; *Magagi*

272 *and Barros*, 2004; *Riehl*, 1959; *Webster*, 1983].

273   During the summer months, the thermal field of the Tibetan Plateau and the resulting

274 strong pressure gradient modify the primary westerly winds that are characteristic of these

275 latitudes to a southeasterly wind system in northeastern India and the realm of the Bay of Bengal

12

276   [*Flohn*, 1957; *Hahn and Manabe*, 1975]. Thus, the precipitation source during the Indian

277   Summer Monsoon (ISM) for the eastern and central southern Himalayan front is the Bay of

278   Bengal, where monsoonal vortices are formed and move to the north and northwest [*Bookhagen*

279   *et al.*, 2005b; *Lang and Barros*, 2002]. These vortexes are released during the active phase of the

280   monsoon and initiate heavy orographic rainfall when colliding with the mountain front [*Barros*

281   *et al.*, 2004; *Bookhagen and Burbank*, 2006; *Galewsky*, 2009]. Overall, the cumulative effect of

282   all vortexes during the active phase of the monsoon results in generally wetter regions in

283   Bangladesh, eastern India, and the central and eastern Ganges plains (Figures 4A and 5). The

284   influence of ISM rainfall (and thus the influence of individual vortexes) decreases rapidly west

285   of ~77° E in the vicinity of the Sutlej Valley and Garhwal Mountains [*Barros et al.*, 2004;

286   *Bookhagen et al.*, 2005b; *Bookhagen and Burbank*, 2006]. In this western region, rainfall is

287   dominated again by westerly and southwesterly wind systems with water vapor originating from

288   the Arabian Sea and possibly as far away as the Mediterranean [*Barros et al.*, 2006; *Hatwar et*

289   *al.*, 2005] (Figures 4 and 5).

290   During the winter months, the temperature gradient reverses with abnormally cold

291   areas on the Tibetan Plateau versus the warmer surrounding oceans. At this time, a pressure

292   gradient develops that results in general northeastern wind systems [*Wang*, 2006]. However, the

293   overall weaker monsoon-related circulation patterns allow the influence of other synoptic

294   circulation systems. In the Himalayan regions of northwest India and Pakistan, the Western

295   Disturbances are the primary weather system responsible for wintertime rainfall and are

296   westerly upper-tropospheric synoptic-scale waves [e.g., *Barros et al.*, 2006; *Dimri*, 2006;

297   *Hatwar et al.*, 2005; *Lang and Barros*, 2004; *Wang*, 2006]. These waves are trapped and

298   intensified by the large-scale topographic features, most notably the notch formed by the

13

299   Himalaya and Hindu Kush mountains in the western syntaxis and the Himalaya and Burmese

300   mountains in the eastern syntax. Thus, the overall rainfall distribution during the winter season

301   significantly changes, and both Himalayan syntaxes receive more precipitation from winter

302   disturbances than the central parts along the Himalayan front (Figure 5B).

303   Generally, the northward push of water vapor is limited by the High Himalayan

304   mountain chain with peaks above 7 km, although some precipitation migrates up large

305   Transhimalayan river valleys onto the Tibetan Plateau. Orographic barriers of the Lesser and

306   Higher Himalaya result in a precipitation-soaked Himalaya, while the regions north of the

307   orographic barriers receive little precipitation (Figure 4A) [*Barros et al.*, 2006; *Barros et al.*,

308   2004; *Bookhagen and Burbank*, 2006; *Galewsky*, 2009].

309   **4.   Results**

310   **4.1 Rainfall**

311   In general, two pronounced rainfall gradients dominate the Ganges Plains and

312   Himalaya (Figure 4A): (1) a ~6-fold east-to-west rainfall gradient with high rainfall amounts in

313   the eastern region, closer to the precipitation source of the Bay of Bengal, and (2) a ~10-fold

314   south-to-north rainfall gradient across the Himalayan mountains that has been previously

315   explored [*Bookhagen and Burbank*, 2006]. The development of these characteristic rainfall belts

316   occurs during the summer monsoon (Figure 5A). The first, outer rainfall peak occurs along the

317   southern margin of the Lesser Himalaya within a narrow band of mean elevation (0.9 ± 0.4 km)

318   and of mean relief (1.2 ± 0.2 km, measured within a 5-km radius) [*Bookhagen and Burbank*,

319   2006]. The second, discontinuous, inner band typically occurs along the southern flank of the

320   Greater Himalaya (elevation and relief: both 2.1 ± 0.3 km) [*Bookhagen and Burbank*, 2006].

321   Both rainfall gradients are clearly expressed on the regional, annual-rainfall map

322   (Figure 4A). The summer monsoon period from May to October (6 months) is responsible for

323   >80% of annual rainfall in the Greater Himalaya and Tibetan region (Figure 4B). A slightly

324   lower ratio pertains if the "monsoon" is restricted to the months of June to September (4 months

325   versus 6). Because monsoonal rainfall in the far eastern Himalaya starts earlier and ends later, we

326   include the months of May and October in our calculation. Only the eastern and western syntaxes

327   receive significant amounts of rainfall during the winter season (Figures 4B and 5B).

328   In order to quantify and explore large-scale rainfall patterns, we analyzed a ~400-km-

329   wide and 2500-km-long swath along strike of the Himalaya (Figure 6A) and projected the data

330   onto a straight line. We separated the data both spatially by elevation and temporally by season.

331   When topographically divided, the annual rainfall data reveal a ~6-fold east-to-west rainfall

332   gradient in the Ganges foreland for elevations ≤500 m asl (Figure 6B). The highest volume of

333   rainfall occurs in the eastern regions, closer to the precipitation source: the Bay of Bengal. The

334   western regions of the foreland lie beyond the monsoonal conveyer belt. This distinct rainfall

335   gradient along the foreland lies in striking contrast to rainfall patterns in higher elevations

336   between 500 and 5000 m asl in at least two respects (Figure 6B, C). First, integrated rainfall

337   volumes from orogen-perpendicular swaths in the mountainous regions are ~5 times lower than

338   total amounts on the eastern plains at elevations < 500 m, but become nearly equivalent in the

339   western regions, despite the fact that the highest rainfall rates generally occur in elevated terrain

340   [*Bookhagen and Burbank,* 2006]. Second, our data reveal no significant rainfall gradient along

341   strike within the Himalaya (elevations ≥500 m: Figure 6B, C). Instead, this contrast with rainfall

342   in the foreland emphasizes the different processes leading to rainfall in the mountainous regions:

343   rainfall in the Himalaya responds to orographic controls, whereas rainfall in the foreland is a

344 function of distance from the Bay of Bengal. The integrated rainfall amount in the mountains

345 appears strikingly similar for at least ~1000 km along strike.

346   When separated by season, the rainfall distribution reveals that the strong east-west

347 rainfall gradient in the plains is a summer phenomenon. During the winter season, higher

348 amounts of rainfall-water volume occur primarily in the eastern and western syntaxes and at

349 higher elevations (dashed black lines in Figure 6C).

350   In order to characterize the orographic impact on rainfall distribution, we have extracted

351 fifty 50-km-wide by 300-km-long swaths along the Himalaya (Figure 7A). All swath profiles

352 trend perpendicular to the mountain front: an orientation parallel to our assumed atmospheric

353 transport direction. This parameterization is not entirely correct for all places, because water-

354 vapor supply depends on individual storm tracks that are not always perpendicular to the

355 mountain front [*Barros et al.*, 2004]. Major river valleys are (sub)parallel to our swath profiles,

356 however, and they funnel water vapor and rainfall into the interior, high-elevation parts of the

357 Himalaya.

358   We identified two intrinsic end members of topographic profiles in the Himalaya: (1) in

359 far western and eastern parts of the Himalaya, 50-km-wide swaths reveal that the mean

360 topography rises more or less steadily to an average elevation of 5 km, and relief increases

361 rapidly to amounts above 3 km (Figure 7B); (2) in contrast, particularly in the central and

362 central-western Himalaya, mean topographic profiles are characterized by a two-step

363 morphology of which the outer step corresponds to the Lesser Himalaya and the inner step to the

364 Higher (Greater) Himalaya geologic units (Figure 7C). These two classes of topographic profiles

365 are mimicked by the rainfall distribution, with a single, high peak of up to 6 m/yr for the steadily

366 increasing topography versus two peaks with lower amounts of ~4 m/yr for the two-step

16

367   morphology. Almost every profile can be clearly assigned to one of these two topographic

368   classes. [These two topographic geometries are typically related to the distance of the Main

369   Central Thrust, MCT, from the southern Himalayan mountain front.] Importantly, whereas the

370   position and magnitude of the rainfall peaks varies among swaths during transport of water vapor

371   and rainfall propagation into the orogen, the integrated rainfall amount within the mountains

372   remains strikingly similar along strike of the Himalaya (Figure 6B).

373   **4.2 Rainfall intensities and lightning strikes**

374   In order to compare storm strength along the Himalaya, we have extracted the

375   maximum rainfall intensity measured in mm/hr during the 10-year measurement period (Figure

376   8A). Rainfall intensities do not mimic mean rainfall distributions (Figure 9): whereas mean

377   annual rainfall varies significantly along strike (Figure 7B), rainfall intensities are more similar

378   along strike (Figure 9). Overall, maximum rainfall intensities during the 10-year measurement

379   period are on the order of 60-80 mm/hr in all frontal and low-elevation regions of the Himalaya

380   (Figures 8 and 9). Rainfall intensities associated with the inner rainfall peak at medium

381   elevations in the central Himalaya are somewhat lower: on the order of 40-60 mm/hr (Figure 9).

382   Interestingly, peak rainfall intensities in the central and in the eastern Himalaya are shifted

383   several dozen kilometers northward compared to mean annual rainfall amounts. This shift most

384   likely reflects propagating storm events and is associated with high-intensity storms that trigger

385   hillslope-erosion processes such as debris flows and landsliding.

386   Despite the generally uniform mean annual rainfall along strike (Figure 6B), rainfall

387   intensities in the western and eastern Himalaya associated with a single rainfall peak are 15-30%

388   higher (70-80 mm/hr) than in the central Himalaya (~60 mm/hr), whereas intensities are still

389   lower (~40 mm/hr) within the Nepalese Himalaya at the second, more northerly, high-rainfall

390   band. Importantly, the largest area of high rainfall intensity is in the low-elevation, frontal

391   western Himalaya (Figure 9A).

392   The analysis of the TRMM Lightning Image Sensor (LIS) reveals >10-fold variation in

393   the number of flashes per km^2 per year along strike of the Himalaya (Figure 8B). We use these

394   data as an additional proxy for rain-storm strength because heavy lightning indicates strong

395   convection in an unstable atmosphere. Regions with increased lightning activity are more likely

396   to have intensified convection resulting in more violent rainstorms [e.g., *Petersen and Rutledge*,

397   2001]. Previously, *Barros et al. [2004]* identified the regions of northern India and Pakistan with

398   high lightning amounts. Similarly, *Houze et al. [2007]* describe the western Himalaya as a region

399   with deep convection processes. We support their findings and also identify high lightning

400   amounts in the Marsyandi catchment in central Nepal, in the eastern Himalaya, and to the south

401   of the Shillong Plateau (Figure 8B). The abnormally high amounts in central Nepal are in fact the

402   highest lightning rates within the Higher Himalaya – all other elevated flash rates are located at

403   or near the southernmost Himalayan topographic front. A generally good spatial correlation

404   exists between high rainfall intensities and high lightning rates (Figure 8A and B).

405   TRMM-derived lightning rates indicate a steep west-to-east gradient with highest

406   lightning amounts in the western regions in all elevation slices (Figures 9). On average, lightning

407   rates in the western Himalaya are twice as high as in the central and eastern Himalaya. No

408   significant lightning rates are recorded at elevations above 4 km. Overall, these data suggest a

409   steep, along-strike gradient with generally more violent storms in the west than in the central and

410   eastern Himalaya (Figures 8B and 9). Thus, despite the overall decrease in monsoonal rainfall

411   amount toward the west (Figures 4A and 6B), a westward increase in the apparent intensity of

412   convection and storm strength leads to broad spatial uniformity in maximum rainfall intensity for

413   the frontal, outer rainfall peak (Figure 9).

414   **4.3 River flow: Spatiotemporal contributions of rainfall, snowmelt, and**

415   **evapotranspiration**

416   In order to estimate the spatiotemporal hydrological river flows, we have created

417   simple, but robust snowmelt and evapotranspiration models and combined them with our rainfall

418   estimates. All datasets are based on calibrated satellite data to provide measurements for the

419   remote Himalaya regions. Satellite-input data for our snowmelt and evapotranspiration models

420   have weekly temporal resolutions; the critical, high-spatial resolution rainfall data are robust on

421   monthly timescales and thus we have calculated monthly averages over the 10-year measurement

422   period. In a second step, the three water-balance components are combined into a runoff model

423   defined by the DEM and are accumulated to generate monthly river flows (also referred to as

424   monthly averaged discharges). In general, the river flows calculated from the snowmelt model,

425   evapotranspiration, and rainfall captures very well ($r^2 = 0.95$) the spatial and temporal

426   distribution of a river-gauged network (Figure 3). The Nash-Sutcliff coefficient [*Nash and*

427   *Sutcliffe, 1970*] varies between 0.7 and 0.9 for the 13 control stations, with a mean of 0.82.

428   Importantly, the model accurately produces the snowmelt and rainfall peak for the Indus (Figure

429   10A) and Sutlej Rivers, each of which has a high snowmelt contribution. Here, we emphasize the

430   discharges derived from rainfall and snowmelt contribution – evapotranspiration generally has an

431   impact of only a few percent in the mountainous catchments (Figure 10A, B). Evapotranspiration

432   becomes more important, however, in the low-elevation Himalayan foreland – a region that is

433   not included in this study (Figure DR5).

434   Next, we explore the spatiotemporal variation of snowmelt and rainfall for each of the

435   27 major Himalayan catchments draining to the south (see Figure 1A for locations). As expected,

436   discharge volumes are strongly dependent on catchment size (Table 1 and Figure 11).

437   Interestingly, catchments in the eastern and central Himalaya receive more than ~70% of their

438   annual rainfall during the summer monsoon, whereas catchments beyond the end of the Indian

439   Summer monsoon conveyer belt (west of the Sutlej: catchment #6 in Figure 1, see also Figures 4

440   and 5A) receive high amounts of precipitation from winter westerlies as well (Figure 11). At the

441   Himalaya's eastern end, the Tsangpo / Brahmaputra catchment has the highest discharge,

442   whereas the second largest catchment – the Indus – has a somewhat lower discharge (Table 1).

443   An important distinction between the Himalaya's two largest rivers is that Tsangpo

444   discharge is primarily derived from rainfall (~80%), whereas Indus discharge has a significant

445   snowmelt component (~66%) (Figure 11A). The third largest catchment by area – the Sutlej – in

446   the western Himalaya, has a high snowmelt component (~57%) as well, whereas the third largest

447   catchment by discharge – the Karnali in the central Himalaya – is largely rain-fed (~80%).

448   On an annual timescale, snowmelt provides ~15 to 60% of discharge in the western

449   Himalaya (Indus to Sutlej: catchments #1 to #6 in Figure 1 and Table 1), whereas the central and

450   eastern Himalaya receive less than 20% of their discharge from snowmelt (Figure 11A, Table 1).

451   Importantly, for all Himalayan rivers draining into the Indian Ocean (the Sutlej (#6) to Indus

452   (#1)), the snowmelt contribution is significant (Figure 11A and 13B, Table 1) due to their high

453   winter-snow cover area and low monsoonal rains (Figure 12C). From a seasonal perspective,

454   central and eastern Himalayan catchments receive ~60 to 85% of their annual discharge as

455   rainfall during the summer (May to October) (Figures 11B and 13A and Table 1).

456   The Ravi (#4), Seti (#12), and Wang (#20) catchments are the wettest along the

457   Himalayan front (Figure 12A). However, these catchments are generally smaller and tend to be

458   restricted to the southern, wetter flank of the Himalaya. Ignoring these river basins, spatially

459   averaged annual rainfall rates appear to be almost uniform along the Himalaya with a slight

460   westward-decreasing gradient and with annual averages between 1.5 and ~2.0 m/yr (Figure

461   12A).

462   The seasonal snow cover derived from MODIS satellite data shows a clear, west-to-

463   east gradient (Figure 12C). For the western half of the catchments, the mean elevation increases

464   slightly westward. This elevational trend, when combined with the influence of winter westerlies

465   and more northerly latitudes, results in a higher average snow cover. Interestingly, the summer

466   snow cover shows only a gentle west-east gradient, suggesting similar snow-cover areas

467   throughout the Himalaya.

468   Seasonal contribution of rainfall and snowmelt to annual discharge shows three distinct

469   characteristics (Figures 13 and 14). First, rainfall during the summer season dominates annual

470   discharge in the central and eastern Himalaya (Figures 13B, 14 and DR6D, Table 1). During the

471   pre- and early monsoon season from May to July, more than ~35% of the annual discharge is

472   derived from rainfall in catchments east of the Sutlej River (catchment #6 in Figure 1, Figure

473   13A). Overall, these catchments receive more than ~80% their annual discharge amounts as

474   rainfall between May and October. Second, summer snowmelt dominates discharge in the

475   western Himalaya, west of the Sutlej River (Figures 13B and DR6D). For example, the Indus

476   River catchment receives 40% (Sutlej: 27%) of its annual discharge during the 3-month period

477   from May to July. On average, catchments west of the Sutlej receive more than 30% of their

478   annual discharge amounts as snowmelt between May and October (Figure 13B, Table 1). In all

479   other Himalayan catchments except for the Tsangpo / Brahmaputra, the snowmelt contribution

21

480   between May and October is <15% of the annual discharge (Figure 13B, Table 1). Third, river

481   flow in the pre- and early monsoon season from March to June includes a large snowmelt

482   contribution, ranging from 30 to ~60% across all Himalayan catchments.

483   **4.4 Testing the validity of discharge predictions**

484   In an attempt to more accurately account for the influence of diverse factors on runoff,

485   we have analyzed discharge measurements along the Sutlej Valley (western Himalaya,

486   catchment #6 in Figure 1) [*B.B.M.B.*, 2000; *Bookhagen et al.*, 2005b]. There, we have three

487   reliable discharge sites located between the Tibetan Plateau and the southern part of the

488   catchment (Figure 15). The higher elevation stations are most influenced by snowmelt, whereas

489   the gauging stations in the middle Sutlej Valley are influenced by both rainfall and snowmelt; the

490   lowest elevations have a significant rainfall component and vegetation cover that leads to

491   generally higher evapotranspiration. For all cases, our discharge model predicts the measured

492   discharge equally well (Figure 15) (cf. Figures DR7 and DR8). Importantly, our discharge model

493   also succeeds in predicting measured snowmelt contributions from several gauged catchments in

494   the Himalaya [*Agarwal et al.*, 1983; *Singh and Quick*, 1993*; Singh et al., 1997*].

495   Evapotranspiration plays only a minor role in the high-elevation, mountainous

496   catchments and is generally less than 10% of the total hydrological budget, with a few exceptions

497   of small, densely vegetated, and low-elevation catchments (Table 1 and Figure DR5).

498   Importantly, evapotranspiration amounts in the Ganges foreland (not included in this analysis but

499   shown in Figure DR5) are up to 30% of rainfall amounts [*Mu et al.*, 2007]. Thus, hydrological

500   studies including the Ganges and Indus foreland must include evapotranspiration as a significant

501   factor within the overall hydrological budget.

502   Generally, our discharge model successfully predicts both the magnitude of the

22

503   discharge and the timing of discharge peaks (Figures 10 and 15). Overall, we argue that, despite

504   our model's simplicity, we are able to capture the main components of the hydrological budget

505   of the mountainous Himalaya. Only the combination of the calibrated, high-spatial resolution

506   TRMM rainfall, the MODIS-derived snowmelt model, and MODIS-derived evapotranspiration

507   amounts allows accurate prediction of discharge amounts. The 10-fold, north-south rainfall

508   gradient across the Himalaya and the spatially varying snow cover render lower resolution data

509   much less useful.

510   **5.   Discussion**

511   **5.1 Limits of remotely-sensed boundary conditions**

512   The Himalaya is part of the largest and the highest mountain chain on Earth. Their

513   terrain is hard to access, and it is almost impossible to build a hydrological dataset based on

514   presently available field data. Thus, we have used several calibrated remotely sensed datasets to

515   constrain the controlling factors for the hydrological budget. Despite our usage of high spatial

516   resolution data and incorporation of new remote-sensing datasets, several shortcomings in the

517   remote sensing data warrant attention when interpreting the results:

518   (1) Our data have been derived on spatial scales of ~5x5 km (rainfall) and ~1x1 km

519   (snowmelt model, evapotranspiration, solar radiation). This resolution places a natural limit on

520   the minimum catchment area that can be studied and accurately resolved with these data

521   (approximately 100 km^2). An additional limit related to the spatial resolution is the areal extent

522   of the data and their dependence on terrain slope; steep terrain has a larger surface area than flat

523   terrain.

524   (2) The temporal resolution of the data does not provide continuous observations like

525 those derived from *in-situ* field measurements, but rather yields one to several snapshots per day.

526 Given that convective rainstorms in the Himalaya have a relatively short lifetime of a half hour

527 to several hours, the data need to be averaged over several weeks or at month-long timescales to

528 provide statistically robust rainfall amounts. Thus, we have limited our high-spatial resolution

529 rainfall data to mean monthly rainfall amounts averaged over the past 10 years. We emphasize

530 that seasonal variation (Fig. 13A) may skew this relationship and may explain some of the scatter

531 shown in the calibration processes (Figure 2). In addition, we caution that our temporal

532 precipitation sampling may miss short, but intense storm events and, therefore, our estimates are

533 considered as minimums. Whereas our data represent a significant improvement in the spatial

534 realm over previously used data, they have clear temporal limitations. Previous research has

535 shown that larger catchments ($>5\times10^3$ km^2) are not significantly affected by rainfall-sampling

536 errors [*Steiner et al., 2003; Nijssen and Lettenmaier, 2004*]. In addition, recent research indicates

537 that the sampling frequency of the raw, orbital TRMM Precipitation Radar is sufficiently rapid to

538 accurately capture steep rainfall gradients [*Nesbitt and Anders, 2009*].

539 (3) Similar constraints exist for the observational spatiotemporal scales for the MODIS

540 products. Because dense cloud cover or high water-vapor content in the atmosphere renders

541 some measurements unreliable, we have used data products that average over an 8-day period,

542 which we then smooth to yield monthly averages.

543 (4) The snowmelt model uses a simple approach to estimate snow-water volumes.

544 Whereas this approach has been shown to be a useful estimator, it certainly neglects several key

545 aspects, such as the distinction between snow and ice (glaciers). However, the contribution of ice

546 melt is in many cases of lesser importance than snowmelt. We have estimated ice-cover extent in

547 the Himalaya with multispectral satellite imagery and identify glacial coverage to be on average

548   10 to 15% of the snowcover area. In addition, we use the same restricted conversion factor (a_r in

549   Equation 1 and 2) throughout the Himalaya. One could refine this approach by creating spatially

550   varying conversion factors. Such conversion, however, requires rigorous calibration efforts with

551   river-gauge stations and measurements near snow-covered or glacierized areas. In the Himalaya,

552   only a few useful river gauges exist because most of the rivers have no measurements at all or

553   have hydropower projects with large dams that alter the water flow, time lag, and

554   evapotranspiration amounts. Whereas our model predicts measured discharge quite well (Figures

555   3, 10, and 15), our station data provide only limited control on the relative influence of snow-

556   versus rain-fed catchments (Figure 15).

557   (5) Our hydrological budget approach includes only rainfall, snowmelt, and

558   evapotranspiration as key components. Whereas these processes are likely to dominate, we

559   neglect transient water storage in soils, floodplain, and vegetation, infiltration (losses to the

560   ground), and ground-water fluxes. These and other processes may be important on smaller

561   spatial and shorter temporal scales.

562   **5.2 Factors that control the rainfall distribution**

563   Previously, we demonstrated a spatial correlation of elevation or relief with the

564   position of the outer and inner Himalayan rainfall peaks [*Bookhagen and Burbank*, 2006].

565   Illustrated by three key observations, the analysis presented here suggests that not only rainfall

566   peaks, but also Himalayan rainfall distributions, are closely related to topography and relief.

567   First, integrated rainfall amounts along the mountainous Himalaya do not vary significantly,

568   despite the strong east-to-west rainfall gradient along the foreland (Figure 6B). Thus, the

569   integrated rainfall content (or total water volume) is similar for the two characteristic

570   morphologies of the southern Himalayan front, even though peak rainfall amounts associated

571 with the steep, one-step morphology are higher and on the order of 4-6 m/yr (Figures 7 and 8).

572 Second, high-relief areas in parts of the western and eastern Himalaya (i.e., in the vicinity of the

573 Chenab, Ravi, Amo, Wang, and Puna Tsang catchments) occur along the southern edge of the

574 Himalayan topography (Figure 7). These high-relief areas result in high amounts of rainfall at the

575 mountain front. When relief within a 5-km-radius circle exceeds 2 km at or near the mountain

576 front, much of the monsoonal precipitation appears to be efficiently extracted, thereby inhibiting

577 the formation of a second, more northerly rainfall peak. Thus, the high amount of rainfall in the

578 low-elevation plains in the eastern and western Himalaya is related to the "barrier of relief" that

579 prevents rainfall from penetrating farther into the orogen. Third, the high amount of rainfall in

580 the Higher (Greater) Himalaya in the central Himalaya (i.e., the Kali Gandaki #11, Seti #12, and

581 Marsyandi #13 in Figure 12) is related to at least two factors: (i) the topographic relief both at the

582 mountain front and of the Lesser Himalaya overall is lower, allowing more water vapor (and

583 ultimately rainfall) to penetrate into the orogen, and (ii) topographic relief of the Greater

584 Himalaya in these regions is unusually high (more than 4 km as opposed to just above 3 km in

585 equivalent regions to the east and west: Figure 7).

586　　　We are able to use topographic (elevation and relief) data to assess the effectiveness of

587 Himalaya-rainfall extraction at a topographic barrier. In order to calculate a rainout ratio

588 perpendicular to the mountain front, we assume that the total rainfall amount is the sum of all

589 TRMM-derived rain in the mountains, i.e., above 500 m elevation. The rainout ratio is somewhat

590 similar to the drying ratio described by *Smith and Evans* [2007], which is defined as the fraction

591 of the incoming water vapor flux that is rained out over the mountains. Because we can not

592 directly measure atmospheric moisture, we refer instead to "rain water," which constitutes the

593 summed TRMM-derived rainfall that occurs downwind of any point in a swath. We calculate a

594 rainout ratio for each rainfall peak within the fifty, 50-km-wide swaths (swath locations are

595 shown in Figure 7A). The rainfall peak defines the center of a 50-km-long area (25 km on each

596 side) under which we integrate rainfall (i.e., rainfall loss from the atmosphere), as well as

597 average topographic elevation and 5-km-radius relief amounts. The rainout ratio for each 50-km-

598 long area is thus the amount of rainfall within the area divided by the total amount of water in the

599 air column (at the upwind edge of that area) that will ultimately be rained out within any swath.

600 This ratio captures the efficiency of rainfall extraction within the rainfall peak and may provide

601 an initial step towards quantifying a topography-rainfall relation. We find a robust relation

602 between the rainout ratio and relief (Figure 16) suggesting that higher relief results in higher

603 rainout ratios: an increase in relief by 1 km results on average in a rainout-ratio increase of

604 ~25%. This rainfall-relief relation appears valid along the southern Himalayan front and explains

605 the variations in peak-rainfall magnitudes along strike (Figures 4A and 7): generally, relief

606 amounts and rainfall at the range front are higher in the eastern and western Himalaya than in the

607 central part of the range [*Bookhagen and Burbank*, 2006].

608   We recognize that rain falls over Tibet beyond the end of our swaths. To the extent that

609 Tibetan rainfall derives from storm paths that trend across the Himalaya from the foreland, our

610 calculations underestimate the total amount of rainwater at the upwind end of a swath and,

611 therefore, overestimate the efficiency of rainfall extraction within the swath. Given the multiple

612 potential sources for rainfall and the overall small amount of total Himalayan-Tibetan rainfall

613 that is represented by rainfall over Tibet, we argue that our simplified treatment, in which we

614 consider only measured rainfall within a swath, is justified.

615 **5.3 Spatial and temporal rainfall and snowmelt variability: implications for erosion**

616   Recent studies suggest that both annual rainfall and its temporal distribution modulate

617   erosion rates [e.g., *Snyder et al.*, 2003]. This dual dependency results because erosion of

618   channels and hillslopes is in many cases a threshold phenomenon: a minimum rainfall intensity

619   must be surpassed before erosion takes place; and high intensity events contribute

620   disproportionately to erosion [e.g., *Gabet et al.,* 2004; *Lague et al.*, 2005; *Snyder et al.*, 2003;

621   *Whipple*, 2004]. We show here that (i) maximum rainfall intensity and lightning frequency

622   generally co-vary spatially and (ii) zones of maximum intensity do not necessarily correlate with

623   zones of high annual rainfall. Notably, the largest area of high intensity rainfall occurs in the

624   northwest Himalaya (Figure 8) where the average monsoonal rainfall (Figures 4 and 12) is

625   considerably less than in the central Himalaya. These high-intensity storms in the NW Himalaya

626   have the potential to sustain rapid erosion, despite the overall drier climate.

627   Interannual variability in precipitation has differing effects depending on a catchment's

628   position along the Himalayan front. For example, we identify the Sutlej valley (catchment 6 in

629   Figures 11, 12, and 13) as a transition zone in the Indian summer monsoon circulation system,

630   where rainfall transported westward from the Bay of Bengal becomes less dominant. *Barros et*

631   *al.* [2004] made similar observations, but suggested that the transition occurs ~150 km farther

632   east near the Garhwal Himalaya in the vicinity of the Ganges valley. Irrespective of any direct

633   link to rainfall, the large-scale Himalayan morphology changes to the west of the Sutlej Valley,

634   such that high topographic relief is developed at the mountain front (Figure 7). This relief

635   prevents the formation of an interior, second rainfall belt, thereby creating a rainfall pattern

636   similar to that which we observe in the vicinity of Bhutan.

637   Where peak rainfall amounts occur in conjunction with steep topography, the resulting

638   runoff is likely to impact erosion on the southern flank of the Himalaya and at the southern edge

639   of the Lesser and Greater Himalayan Sequences. Evidence from both weak and strong monsoon

640   years indicates that these rainfall peaks are spatially stationary [*Bookhagen et al.*, 2005a;

641   *Bookhagen and Burbank*, 2006]. During large storms, however, more rainfall penetrates into

642   drier areas, and the magnitude of the average, south-to-north rainfall gradient is decreased

643   [*Craddock et al.*, 2007; *Wulf et al., in press*]. Our TRMM-derived rainfall intensity

644   measurements support this finding. Previously, we showed that large, synoptic storms during

645   stronger monsoon years enhance the rainfall in the high-elevation areas [*Bookhagen et al.*,

646   2005a; *Wulf et al.*, in press]. Similarly, the intensified monsoon phases during the early Holocene

647   are interpreted to have swept more rainfall and water vapor into the high-elevation regions

648   [*Bookhagen et al.*, 2005a; *Bookhagen et al.*, 2005b; *Gasse et al.*, 1991; *Pratt et al.*, 2002]. To the

649   extent that high topographic relief exists in the Himalayan rain shadow, our relief-rainfall

650   analysis (Figure 16) suggests that this relief will tend to focus precipitation in specific regions

651   [*Brozovic et al.*, 1997]. Thus, during intensified monsoon periods, the resultant enhanced

652   discharge should mobilize more sediment and augment erosion rates within these normally arid

653   regions [*Bookhagen et al.*, 2006; *Wulf et al.,* in press]. Overall, in times of strengthened

654   monsoons, we suggest a change of the 'rainfall-tail length' that will enhance rainfall and

655   probably erosion several fold in the high-elevation, high-relief (and usually dry) areas, but will

656   not change the location of major peaks in rainfall along the southern flank of the Himalaya.

657   Our snowmelt model indicates that the annual snowmelt contribution to discharge is

658   most pronounced in the high elevations of the western Himalaya, as well as in a dozen-

659   kilometer-wide swath encompassing the high summits of the main Himalayan chain (Figure

660   14B). The southern parts of the Himalayan catchments receive most of their annual hydrological

661   budget as rainfall during summer months. Large quantities of water are stored in the form of

662   snow in the high elevation and western parts of the Himalaya and their release does not occur

663   until several months later in the pre- and early monsoon season. This rapid release of meltwater

664   from March to June leads to serious flooding problems in the Ganges foreland [*e.g., Sharma et*

665   *al.*, 1991].

666   Three dominant factors modulate snow accumulation and areal cover (Figure 17): (1)

667   the elevation distribution within a catchment (hypsometry); (2) the magnitude of precipitation;

668   and (3) the seasonality of precipitation (temporal distribution of precipitation). Higher

669   topography experiences lower temperatures, greater proximity to the peak precipitation leads to

670   greater total precipitation (some of which will fall as snow), and a higher fraction of winter

671   precipitation within the annual cycle all promote more snow accumulation and areal cover.

672   Notably, in comparison to summer storms, dampened convection during winter storms reduces

673   the efficiency of rainfall extraction by topography (rainout ratio: Figure 16) and, consequently,

674   reduces orographic effects, such that winter snowfalls are both more areally extensive and

675   uniform in amount [*Putkonen*, 2004; *Wulf et al., in press*]. The distinctive hypsometry of the two

676   large western catchments (Indus, Sutlej) in conjunction with their relatively high winter

677   precipitation supply results in large snow accumulation and expansive snow cover. In contrast,

678   the hypsometrically similar Arun catchment in the central Himalaya is monsoon-dominated,

679   receives lower winter precipitation, and, therefore, displays an areally restricted snow cover.

680   **6.   Conclusion**

681   We combine several new datasets in an attempt to increase our understanding of the

682   spatiotemporal discharge distribution across the Himalaya. First, we analyzed 10 years of high-

683   resolution rainfall data from the Tropical Rainfall Measurement Mission (TRMM) to create an

684   unprecedented overview of modern, spatiotemporal variations in Himalayan monsoonal

685   precipitation. We improved our processing algorithms of orbital data to re-project all swaths onto

686   an equally-spaced grid. After this correction and calibration with more than 1700 rain gauges, a

687   coherent rainfall map emerges for the entire Himalaya. When we separate seasonal rainfall

688   amounts and quantify rainfall gradients, two striking gradients emerge: a six-fold east-to-west

689   rainfall gradient along the Himalayan foreland; and a ten-fold south-to-north gradient across the

690   Himalayan range. From a seasonal perspective, most of the Himalaya and Tibet receive more

691   than 80% of their rainfall during the Indian summer monsoon from May to October, but the

692   eastern and western syntaxes, where the Tsangpo and Indus rivers exit the range, receive

693   significant precipitation during the winter months as well. The seasonal east-to-west rainfall

694   gradient divides near the Sutlej valley in the western Himalaya: all catchments to the east (and

695   thus all catchments draining into the Bay of Bengal) receive ~70% of their annual rainfall during

696   the Indian Summer Monsoon (June to September). All catchments to the west of the Sutlej

697   receive less than 50% of their annual rainfall during the summer months (Figure 18).

698   Second, we show that rainfall within the Himalaya itself– despite strong rainfall

699   gradients along the foreland – is dominated by topography. Whereas the total amount of rainfall

700   that penetrates into the mountainous Himalaya remains nearly constant along strike, the spatial

701   rainfall distribution within the mountains varies widely. We identify two topographic end

702   members (steadily rising versus stepped topography) that correlate with either a single rainfall

703   peak at the range front or two rainfall peaks: one at the range front and one near the toe of the

704   Greater Himalaya. We conclude that topographic relief reliably predicts the efficiency of rainfall

705   extraction within the Himalaya: higher relief causes a higher rainout rate.

706   Third, we have used the Lightning Image Sensor (LIS) onboard the TRMM platform to

707   create the first coherent lightning map of the Himalaya and to identify regions in the Himalaya

708   with abnormally high lightning activity. These areas indicate vigorous atmospheric convection

709   and generally correlate with intense storm events. In Pakistan and NW India, both the far western

710   frontal region and the medium-to-high elevation Himalayan regions have some of the highest

711   documented lightning rates on Earth with more than 65 lightning strikes per km^2 per year. Rates

712   almost as high are observed just south of the Shillong Plateau, one of the wettest places on Earth.

713   The general spatial pattern of the lightning rates is mimicked by a rainfall intensity map that

714   shows maximum hourly rainfall intensities during the 10-year period. Despite along-strike

715   variations in mean annual rainfall, average rainfall intensities remain rather constant. In the outer

716   rainfall band along the Himalayan front, intensities are on the order of 60-80 mm/hr, regardless

717   of the mean rainfall amounts. Rainfall intensities of the inner rainfall peak in the central

718   Himalaya are generally lower: ~30 to 60 mm/hr. We show that extreme rainfall events (relative

719   to average local rainfall) are more common in drier areas. Thus, during strengthened monsoons,

720   southern Tibet is expected to receive both more common and more intense storms, even though

721   the zones of highest rainfall will remain spatially stationary on the southern Himalayan flank.

722   Fourth, we create a simple, but robust snow-runoff model based on satellite-derived

723   data. This model relies on MODIS-derived snow cover and temperature data, and it includes a

724   solar radiation component calculated from the digital topography. The snowmelt model is a

725   significant step forward in regional runoff modeling for the Himalaya because it assigns a snow

726   cover, temperature, and solar radiation value to each grid cell and does not require subdividing

727   the catchment into areas with similar climatic properties.

728   Fifth, we combine the snowmelt model with the TRMM-derived rainfall and MODIS-

729   derived evapotranspiration measurements into annual and seasonal river-flow estimates. We

730   show that snowmelt accounts for ~50% in the annual runoff budget in the western Himalaya

731   (Indus, Sutlej) (Figure 18). In contrast, the generally smaller central and eastern Himalaya

732 catchments receive more than 80% of their annual runoff from rainfall and less than 20% from

733 snowmelt (except the large Tsangpo / Brahmaputra catchment which receives ~34% of its annual

734 discharge from snowmelt). Despite the eastward decrease in the contribution of snowmelt to

735 annual runoff, snowmelt is significant and important for all catchments in the pre- and early

736 monsoon months from March to June. During this time, more than 40% of the discharge is

737 derived from snowmelt and is vital to agriculture, hydropower, and water quality throughout the

738 Himalayan foreland.

739 **7. Acknowledgements**

746

747 **Tables**

#	Catchment (*Country*)	Size (km^2)	mean annual 2B31 rainfall (m/yr)	mean annual discharge (rain+snow-ET) x10^3 (m^3/s)	snowmelt contribution to annual discharge (%)	Evapotranspiration (ET) contribution to annual discharge (negative contribution in %)	May-Oct rainfall contribution to annual discharge (%)	May-Oct snowmelt contribution to annual discharge (%)
1	Indus (*Pakistan*)	205,536	0.3	4.2	65.7	2.2	26.2	61.6
2	Jhelum (*India*)	26,539	1.3	1.2	24.9	17.1	65.1	17.7
3	Chenab (*India*)	21,901	1.1	1.1	43.4	7.6	43.5	38.2
4	Ravi (*India*)	5,562	2.4	0.4	16.1	9.0	59.1	10.2
5	Beas (*India*)	7,644	2.0	0.5	21.3	9.0	64.9	16.5
6	Sutlej (*India*)	52,798	0.3	0.8	57.1	5.3	38.1	48.3
7	Tons/Yamuna (*India*)a	10,235	2.0	0.6	9.8	17.0	88.9	4.7
8	Ganges (*India*)	21,731	1.4	1.1	22.4	12.3	75.0	18.2
9	Mahakali (*India/Nepal*)	15,216	1.8	0.8	14.4	15.2	83.6	11.3
10	Karnali (*Nepal*)	45,529	1.2	1.8	20.5	14.2	80.9	14.3
11	KaliGandaki (*Nepal*)	11,863	2.0	0.7	10.0	11.9	87.7	7.2
12	Seti (*Nepal*)	2,943	3.2	0.3	2.8	11.8	92.7	1.6
13	Marsyandi (*Nepal*)	4,805	2.0	0.3	15.1	7.1	74.3	11.4
14	Trisuli (*Nepal*)	11,688	1.6	0.6	15.0	6.5	78.8	10.3
15	Sunkosi (*Nepal*)	18,182	1.9	1.1	8.6	7.7	79.3	6.3
16	Arun (*Nepal*)	33,578	0.5	0.6	24.7	5.5	69.2	19.4
17	Tamur (*Nepal*)	6,102	1.8	0.3	7.1	10.3	90.6	4.7
18	Tista (*Nepal*)	8,166	1.9	0.5	8.2	9.1	86.9	5.3
19	Amo (*Nepal/Bhutan*)	3,285	2.0	0.2	10.5	8.1	80.9	5.8
20	Wang (*Bhutan*)	4,597	2.3	0.3	8.4	7.3	89.1	4.1
21	PunaTsang (*Bhutan*)	9,688	1.6	0.5	10.4	10.2	90.2	6.4
22	Mangde/Chamkhar (*Bhutan*)	7,432	1.5	0.4	10.4	12.4	90.5	6.2
23	Manas (*Bhutan*)	21,061	0.8	0.6	24.6	10.9	75.7	17.0
24	Bhareli (*India*)	9,526	1.6	0.5	9.1	17.9	91.9	5.5
25	Subansiri (*India*)	26,245	1.3	1.1	13.6	11.5	79.4	7.7
26	Tsangpo (*India/China*)	255,929	0.5	5.1	34.3	4.1	59.2	29.1
27	Dibang (*India*)	11,271	2.2	0.8	8.6	4.8	70.4	4.4
Average (per catchment)			1.6	1.0	19.2	9.9	74.5	14.6
Average for all 27 Himalayan catchments					30.4	8.0	63.0	25.5

748 Table 1

749 Table 1: Spatial and hydrologic overview and summary of all 27 major southern Himalayan
750 catchments (see Figure 1A for locations). Catchments 1 to 6 drain into the Arabian Sea,
751 while all other catchments drain into the Bay of Bengal. Generally, catchments in the far
752 western and somewhat in the eastern Himalaya have a higher snowmelt contribution to
753 discharge then central Himalayan catchments. Negative contribution of evapotranspiration

34

754   (ET) to annual discharge is linked to catchment vegetation amounts and usually <10%,
755   except for a few, smaller, densely vegetated catchments. Note that rainfall during the
756   summer monsoon (May to October) accounts for ~63% of the annual discharge from the
757   entire Himalaya. In contrast, snowmelt mostly during the early summer season accounts
758   for ~25% of the annual discharge from the Himalaya.

759

Figure Captions

760

761 Figure 1: (A) Topographic map showing the study area and the 27 major catchments draining the
762 Himalaya to the south. White circles indicate river-discharge stations with daily measurements and labels
763 mark reference catchments and river names. (B) Shaded-relief topography and daily rain-gauge locations
764 used for TRMM rainfall calibration (n = 1741). Note the high-elevation stations in western India, central
765 Nepal, and Bhutan.

766

767 Figure 2: Calibration of 10-year mean annual TRMM 2B31 data with 1741 stations throughout the
768 Himalaya and foreland (see Fig.1B for locations). Rainfall intensities are linearly related with gauged
769 rainfall over more than an order of magnitude (y=10.72±0.13*x; ±95% confidence interval). TRMM2B31
770 values are weighted with RMS estimates from TRMM product 2B31 (Sigma-RR-Surf). High-amount
771 rainfall stations (> 10 m/yr) are from south of the Shillong Plateau. For statistical rigor, we have performed
772 the same calibration with high rainfall intensities (>6 m/yr) removed; the predictive relation remains
773 statistically identical. The ordinate displays mean annual-rainfall intensity for each rainfall-station pixel
774 and was derived from TRMM product 2B31 (RR-Surf).

775

776 Figure 3: Validation results of discharges derived from rainfall, snowmelt modeling, and
777 evapotranspiration. We have used 13 stations that recorded daily discharge amounts during our modeling
778 period (2000 to 2007) throughout the Himalaya. We show measured mean-monthly discharge (n = 12
779 months x13 stations = 156) vs. error weighted mean-monthly model outputs. Shading indicates the 95%
780 confidence intervals for the linear regression. The Nash-Sutcliffe coefficients are between 0.7 and 0.9
781 with a mean at 0.82 for the 13 control stations. The bold, dashed line indicates a 1:1 relation. On average,
782 our weighted fit of the runoff model slightly overpredicts discharge amounts by ~3±5%. The TRMM 2B31
783 rainfall (without a snowmelt and evapotranspiration component) underpredicts discharge on average by
784 ~40±8% (with values of 60% and more during the summer months). Locations of river-gauge stations are
785 shown in Figure 1A.

786

787 Figure 4: A. Mean annual rainfall based on calibrated TRMM 2B31 data and averaged over 10 years from
788 1998 to 2007. Note the formation of an outer and inner rainfall band at the main topographic barriers of
789 the Himalaya. B. Percentage of summer rainfall (May to October) versus annual rainfall. Most Himalayan
790 and Tibetan areas receive more than 80% of their annual rainfall during the months from May to October.
791 Only the syntaxes and western Himalaya receive significant rainfall amounts during the remainder of the
792 year (November to April). Note the artifactual effect where the two rainfall datasets (TRMM 2B31 and
793 3B42) are merged at 36°N latitude (see text for explanation).

794

795 Figure 5: Seasonal rainfall during the Indian Summer Monsoon from May to October (A) and during the
796 winter season (November to April, B) Note the different scales used for the rainfall amounts; color of the
797 highest winter rainfall match intermediate (1-2 m/yr) summer rainfall amounts. Rainfall during the summer
798 season shows a pronounced east-west gradient in the Ganges plain, with higher amounts (> 4 m/yr)
799 occurring at the topographic barriers. The two-peak rainfall belt primarily develops during the summer
800 season. In contrast, rainfall distribution during the winter season indicates that primarily the syntaxes
801 receive rainfall through large-scale circulation patterns.

802

803 Figure 6: A. Location map of the 400-km-wide, 2500-km-long rainfall swath following the Himalayan arc.
804 All topographic and climatic data have been projected onto a straight line. B. Annual rainfall amounts in all
805 areas with (1) elevations <500 m (i.e., the Ganges Plain) (2) elevations between 500 and 5000 m asl (i.e.,
806 the mountainous Himalaya). Note the strong east-west gradient on the Ganges Plain (elevations <500 m
807 asl) and high rainfall amounts in the eastern Himalaya, closer to the Bay of Bengal moisture source.
808 Despite the strong rainfall gradient along the foreland, areas at elevations >500 m receive a nearly

809 constant water volume between 400 and 1800 km along-strike. C. Seasonal rainfall, where black dashed
810 lines outline the winter season (November to April) rainfall. During winter, the slight increase in rainfall-
811 water volume in the eastern and western area reflects winter storms that drive rainfall into the higher
812 elevation areas. The greatest overall rainfall amounts in the higher elevated, eastern Himalaya are related
813 to the Shillong Plateau.

814

815 **Color Caption** Figure 7: A. Location of numbered 50-km wide and 300-km long swaths used to illustrate
816 two topographic, relief, and rainfall-distribution end members. B. Steadily rising topographic profile results
817 in a single high-amount rainfall peak (swaths used are those shown by white polygons in location map A).
818 5-km-radius relief is indicated by the orange lines. C. Two-step morphology coinciding with the Lesser
819 Himalaya units and Higher (Greater) Himalaya forming two rainfall peaks (swaths are gray polygons in A).

820 **B&W Caption** Figure 7: A. Location of numbered 50-km wide and 300-km long swaths used to illustrate
821 two topographic, relief, and rainfall-distribution end members. B. Steadily rising topographic profile results
822 in a single high-amount rainfall peak (swaths used are those shown by white polygons in location map A).
823 5-km-radius relief is indicated by the dashed lines. C. Two-step morphology coinciding with the Lesser
824 Himalaya units and Higher (Greater) Himalaya forming two rainfall peaks (swaths are gray polygons in A).

825

826 Figure 8: A. Maximum rainfall intensity (mm/hr) during the 10-year measurement period. B. TRMM LIS
827 (Lightning Image Sensor) mean annual lightning rates, averaged over the same time period. Both
828 datasets were smoothed by a 25x25 km (5 pixel) window. Generally, high rainfall intensities correlate with
829 orographic barriers, but the western (NW India, Pakistan) and eastern Himalaya (Bhutan, Shillong
830 Plateau) experience significantly higher intensities than the central Himalaya. These high-intensity areas
831 are prone to flash floods. Note the high lightning rates in these western and eastern areas, underlining the
832 unstable atmospheric conditions. Within the central Himalaya, moderate to high lightning amounts are
833 recorded only in central Nepal.

834

835 **Color Caption** Figure 9: Smoothed rainfall, topography, rainfall intensity and number of lightning events
836 averaged over several swaths for the western (A), central (B), and eastern (C) Himalaya. Bold lines with
837 gray shading indicate mean topography and $\pm 2\sigma$ amounts, blue lines indicate TRMM-derived rainfall (both
838 on left-hand Y axis). Dashed blue lines show maximum rainfall intensity during the 10-year measurement
839 period and red, bold line indicates number of lightning events per km^2 per year (right-hand Y axis). See
840 Figure 8 for swath locations. Note that rainfall intensities are similar between the regions despite the
841 different mean rainfall amounts.

842 **B&W Caption** Figure 9: Smoothed rainfall, topography, rainfall intensity and number of lightning events
843 averaged over several swaths for the western (A), central (B), and eastern (C) Himalaya. Bold lines with
844 gray shading indicate mean topography and $\pm 2\sigma$ amounts, thin lines indicate TRMM-derived rainfall (both
845 on left-hand Y axis). Dashed lines show maximum rainfall intensity during the 10-year measurement
846 period and bold gray line indicates number of lightning events per km^2 per year (right-hand Y axis). See
847 Figure 8 for swath locations. Note that rainfall intensities are similar between the regions despite the
848 different mean rainfall amounts.

849

850 **Color Caption** Figure 10: Characteristic annual hydrographs for the snowmelt-dominated Indus (A)
851 ($\sim 200 \times 10^3$ km^2, #1 in Figure 1) and rain-fed Tista (B) ($\sim 8 \times 10^3$ km^2, #18 in Figure 1) catchments from the
852 western and central Himalaya, respectively. Bold dashed lines indicate mean-monthly discharge
853 measurements and shaded areas show results from modeled discharge (snowmelt plus rainfall). Blue
854 circles indicate discharge from rainfall and orange crosses indicate snowmelt-derived discharges. Green
855 squares show evapotranspiration (ET). Note that ET amounts are negative in the hydrologic-budget
856 equation. Overall, the model successfully mimics the general discharge pattern with Nash-Sutcliffe
857 coefficients of 0.88 (Indus) and 0.86 (Tista). Panel above hydrographs indicates the rain vs. snow
858 contribution in the cumulative sum. Note the temporal discrepancy in rainfall and snowmelt runoff in the

859   Indus catchment: Discharge is dominated by snowmelt in the pre- and early monsoon season, whereas
860   rainfall becomes more important during the mid to late summer.

861   **B&W Caption** Figure 10: Characteristic annual hydrographs for the snowmelt-dominated Indus (A)
862   ($\sim$200x10^3 km^2, #1 in Figure 1) and rain-fed Tista (B) ($\sim$8x10^3 km^2, #18 in Figure 1) catchments from the
863   western and central Himalaya, respectively. Bold dashed lines indicate mean-monthly discharge
864   measurements and shaded areas show results from modeled discharge (snowmelt plus rainfall). White
865   circles indicate discharge from rainfall and crosses indicate snowmelt-derived discharges. Gray squares
866   show evapotranspiration (ET). Note that ET amounts are negative in the hydrologic-budget equation.
867   Overall, the model successfully mimics the general discharge pattern with Nash-Sutcliffe coefficients of
868   0.88 (Indus) and 0.86 (Tista). Panel above hydrographs indicates the rain vs. snow contribution in the
869   cumulative sum. Note the temporal discrepancy in rainfall and snowmelt runoff in the Indus catchment:
870   Discharge is dominated by snowmelt in the pre- and early monsoon season, whereas rainfall becomes
871   more important during the mid to late summer.

872

873   **Color Caption** Figure 11: A. Annual discharge derived from rainfall and snowmelt contributions.
874   Discharge derived from rainfall plus snowmelt minus evapotranspiration is calculated at each catchment's
875   outlet at the Himalayan front from west to east (see Figure 1A for catchment location and Table 1 for
876   catchment characteristics). In all the following figures using the 27-catchment view, the gray band from
877   catchments #10 to #18 indicates catchments within Nepal. Top panel shows rainfall-derived (blue) and
878   snow-melt (orange) discharge. Bold line indicates percentage of rainfall contribution to annual discharge.
879   Discharge is a function of climatic parameters and catchment size. Western catchments receive low
880   rainfall contributions but significant snowmelt contributions. B. Seasonal discharge distribution for the
881   summer (May to October) and winter (November to April) season vs. annual discharge. Summer rainfall in
882   Nepalese catchments accounts for between $\sim$60-85% of the annual discharge. Western catchments
883   receive less than $\sim$50% of their discharge contribution from summer rainfall.

884   **B&W Caption** Figure 11: A. Annual discharge derived from rainfall and snowmelt contributions.
885   Discharge derived from rainfall plus snowmelt minus evapotranspiration is calculated at each catchment's
886   outlet at the Himalayan front from west to east (see Figure 1A for catchment location and Table 1 for
887   catchment characteristics). In all the following figures using the 27-catchment view, the gray band from
888   catchments #10 to #18 indicates catchments within Nepal. Top panel shows rainfall-derived and snow-
889   melt discharge. Bold line indicates percentage of rainfall contribution to annual discharge. Discharge is a
890   function of climatic parameters and catchment size. Western catchments receive low rainfall contributions
891   but significant snowmelt contributions. B. Seasonal discharge distribution for the summer (May to
892   October) and winter (November to April) season vs. annual discharge. Summer rainfall in Nepalese
893   catchments accounts for between $\sim$60-85% of the annual discharge. Western catchments receive less
894   than 50% of their discharge contribution from summer rainfall.

895

896   Figure 12: A. Calibrated TRMM-derived summer (May to Oct), winter (Nov to Apr), and annual rainfall.
897   Central and eastern catchments are dominated by the Indian Summer monsoon (ISM, here June to
898   September and the extended summer season from May to October) with no apparent along-strike rainfall
899   gradient. Note that large parts (>50%) of the Indus, Sutlej, Arun, and Tsangpo catchments lie within the
900   dry Tibetan dry zone. B. Mean elevations (gray shading $\pm 2\sigma$) show little variation along strike (with the
901   exception of the smaller catchments Seti #12 and Bhareli #24), whereas most of the maximum elevations
902   of major peaks occur in the central Himalaya. C. Average fraction of catchment covered with snow based
903   on 8 years of MODIS snow-cover data. Note the general westward increase in snow cover on both a
904   seasonal and annual basis. In combination with reduced rainfall in the western Himalaya (see A), the high
905   snow cover area has a pronounced effect on river discharge (Figure 13).

906

907   Figure 13: Seasonal rainfall (A) and snow-melt (B) contributions to annual discharge. Rainfall during May
908   to July (MJJ) generates 30-40% (in places >45%) of the annual runoff in the central Himalaya. Both early
909   (MJJ) and late summer (August to October, ASO) show a steep gradient with significantly lower
910   contribution in the western catchments. Snowmelt during May to June is an important contribution to the

911 overall annual runoff in western Himalayan and Tsangpo catchments (>10%, and for the Indus, up to
912 40%). Snowmelt during the winter season contributes only ~5% of the annual runoff. Note that
913 evapotranspiration is not subtracted from rain and snowmelt contribution and therefore rain and snowmelt
914 may add up to >100%.

915

916 Figure 14: Spatial distribution of annual snowmelt contribution to discharge. Note the high percentages
917 derived from snowmelt in the western catchments as well as in the high elevations along the Himalaya.
918 The frontal areas are dominated by rainfall and thus have very low snowmelt contribution.

919

920 **Color Caption** Figure 15: A. Sutlej River region (catchment #6 in Figure 1), showing gauging stations 1 to
921 3. Annual hydrographs for the high-elevation, northeastern section of the catchment (site 1: B), the
922 moderate-elevation section (site 2: C), and the low-elevation section (site 3: D). Dashed lines indicate
923 gauged discharge and light gray coloring outlines predicted discharge from the rainfall (blue circles) and
924 evapotranspiration (green squares) data and snowmelt model (orange crosses). Note that
925 evapotranspiration amounts are a negative term in the hydrologic budget. Generally, the model predicts
926 discharges well. (E) Area vs. elevation for the Sutlej River. Note horizontal steps result from tributary
927 junctions. Discharge measurements of gauging stations 1-3 shown on the right axis.

928 **B&W Caption** Figure 15: A. Sutlej River region (catchment #6 in Figure 1), showing gauging stations 1 to
929 3. Annual hydrographs for the high-elevation, northeastern section of the catchment (site 1: B), the
930 moderate-elevation section (site 2: C), and the low-elevation section (site 3: D). Dashed lines indicate
931 gauged discharge and light gray coloring outlines predicted discharge from the rainfall (white circles) and
932 evapotranspiration (gray squares) data and snowmelt model (crosses). Note that evapotranspiration
933 amounts are a negative term in the hydrologic budget. Generally, the model predicts discharges well. (E)
934 Area vs. elevation for the Sutlej River. Note horizontal steps result from tributary junctions. Discharge
935 measurements of gauging stations 1-3 shown on the right axis.

936

937 Figure 16: Relief versus rainout ratio for 50-km-wide swaths (see Figure 8 for swath-profile location).
938 Rainout ratio (ratio of peak-rainfall amounts to upwind volume of rain water in the atmosphere at the
939 upwind end) indicates how much rainfall is lost across a 50-km-long zone that is centered on the highest
940 rainfall peak(s) in each swath. Alternatively, the rainout ratio can be viewed as the fraction of incoming
941 rain water removed in the 50-km-wide peak area. Horizontal lines indicate the 1-sigma standard deviation
942 of relief under the rainfall area. Relief is measured with a 5-km radius for each pixel and averaged across
943 the swath. This correlation suggests that relief is a moderately robust (r^2 = 0.71) indicator for orographic-
944 barrier efficiency. Outer (first) rainfall peaks lose more than 40% of their rainfall in areas with 1.5-2 km of
945 relief, whereas an orographic barrier at the Himalayan front with 3-km relief is predicted to cause an
946 ~80% loss of the upwind rain water (rainout ratio of ~0.8).

947

948 Figure 17: Conceptual summary of the three dominant factors exerting control on snow accumulation and
949 hence snowmelt generation in mountainous regions: (1) Catchment hypsometry or elevation distribution
950 within a catchment, (2) spatial distribution of precipitation magnitude, (3) seasonality or temporal
951 distribution of precipitation. Higher topography, greater proximity to the precipitation peak, and a higher
952 fraction of winter precipitation all lead to more snow accumulation.

953

954 Figure 18: Conceptual climatic and hydrologic model for the Himalaya. Light gray shading of Himalayan
955 catchments primarily in the central and eastern Himalaya indicate snowmelt contribution of <25% to
956 annual discharge. Moderate to high snowmelt contribution occur in catchments with significant winter
957 snowcover (e.g., Indus, Sutlej, Arun and Tsangpo). Black arrows indicate catchment and their
958 corresponding summer (May to October) rainfall amounts: western catchments receive <65% of their
959 annual discharge from rainfall (Indus: 40%), whereas catchments to the east of the Sutlej receive >70% of
960 their annual discharge from rainfall. Gray arrows indicate major moisture-source directions.

961

962   **8.   References**

Agarwal, K. C., et al. (1983), Snowmelt runoff for subcatchment of Beas basin, paper presented at Proceedings First National Symposium on Seasonal Snowcover (April 1983), SASE, Manali, India.

Anders, A. M., et al. (2006), Spatial patterns of precipitation and topography in the Himalaya, *GSA Special Paper*, *398*, 39-53.

Anderson, E. A. (1973), National weather service forcast system, snow accumulation and ablation mode.

Arnold, J. G., and N. Fohrer (2005), SWAT2000: current capabilities and research opportunities in applied watershed modelling, *Hydrological Processes*, *19*(3), 563-572.

B.B.M.B. (2000), B.B.M.B. (Beas Bhakra Management Board) and Jaiprakash Company, New Delhi (India) provided data for hydrological analyses.

Barnett, T. P., et al. (2005), Potential impacts of a warming climate on water availability in snow-dominated regions, *Nature*, *438*(7066), 303-309.

Barros, A., et al. (Eds.) (2006), *From weather to climate—Seasonal and interannual variability of storms and implications for erosion processes in the Himalaya*, 17-38 pp., Geological Society of America Special Paper, Boulder.

Barros, A. P., et al. (2000), A study of the 1999 monsoon rainfall in a mountainous region in central Nepal using TRMM products and rain gauge observations, *Geophysical Research Letters*, *27*(22), 3683-3686.

Barros, A. P., et al. (2004), Probing orographic controls in the Himalayas during the monsoon using satellite imagery, *Natural Hazards and Earth System Sciences*, *4*(1), 29-51.

Bookhagen, B., et al. (2005a), Abnormal monsoon years and their control on erosion and sediment flux in the high, and northwest Himalaya, *Earth and Planetary Science Letters*, *231*(1-2), 131-146.

Bookhagen, B., et al. (2005b), Late Quaternary intensified monsoon phases control landscape evolution in the northwest Himalaya, *Geology*, *33*(2), 149-152.

Bookhagen, B., and D. W. Burbank (2006), Topography, relief, and TRMM-derived rainfall variations along the Himalaya, *Geophysical Research Letters*, *33*(8), 2006GL026037.

Bookhagen, B., et al. (2006), Holocene monsoonal dynamics and fluvial terrace formation in the northwest Himalaya, India, *Geology*, *34*(7), 601-604.

Bookhagen, B., and M. R. Strecker (2008), Orographic barriers, high-resolution TRMM rainfall, and relief variations along the eastern Andes, *Geophysical Research Letters*, *35* (doi:10.1029/2007GL032011). .

Boos, W.R., and Z. Kuang (2010), Dominat control of the South Asian monsoon by orographic insulation versus plateau heating, Nature, 463, 218-222, doi:10.1038/nature08707

Brozovic, N., et al. (1997), Climatic limits on landscape development in the northwestern Himalaya, *Science*, *276*(5312), 571-574.

Brubaker, K., et al. (1996), Incorporating radiation inputs into the snowmelt runoff model, *Hydrological Processes*, *10*(10), 1329-1343.

Burbank, D. W., A. E. Blythe, J. Putkonen, B. Pratt-Sitaula, E. Gabet, M. Oskin, A. Barros, and T. P. Ojha (2003), Decoupling of erosion and precipitation in the Himalayas, *Nature, 426*, 652-655.

Christian, H. J., et al. (1999), The Lightning Imaging Sensor, paper presented at Proceedings of the 11th International Conference on Atmospheric Electricity, Guntersville, Alabama, June 7-11, 1999, .

Clemens, S. C., et al. (1996), Nonstationary phase of the plio-pleistocene Asian monsoon, *Science*, *274*(5289), 943-948.

Clemens, S. C., and W. L. Prell (2003), A 350,000 year summer-monsoon multi-proxy stack from the Owen ridge, Northern Arabian sea, *Marine Geology*, *201*(1-3), 35-51.

Cleugh, H. A., R. Leuning, Q. Z. Mu, and S. W. Running (2007), Regional evaporation estimates from flux tower and MODIS satellite data, *Remote Sensing of Environment*, *106*(3), 285-304.

Craddock, W. H., et al. (2007), Bedrock channel geometry along an orographic rainfall gradient in the upper Marsyandi River valley in central Nepal, *Journal of Geophysical Research-Earth Surface*, *112*(F03007), doi:10.1029/2006JF000589.

Dimri, A. P. (2006), Surface and upper air fields during extreme winter precipitation over the western Himalayas, *Pure and Applied Geophysics*, *163*(8), 1679-1698.

Ding, Y. H., and J. C. L. Chan (2005), The East Asian summer monsoon: an overview, *Meteorology and Atmospheric Physics*, *89*(1-4), 117-142.

Farr, T. G., et al. (2007), The Shuttle Radar Topography Mission, *Rev. Geophys.*, *45*(RG2004), doi:10.1029/2005RG000183.

Fasullo, J., and P. J. Webster (2003), A hydrological definition of Indian monsoon onset and withdrawal, *Journal of Climate*, *16*(19), 3200-3211.

Ferguson, R. I. (1999), Snowmelt runoff models, *Progress in Physical Geography*, *23*(2), 205-227.

Flohn (1957), Large-scale aspects of the "summer monsoon" in south and East Asia, *J. Meteor. Soc. Japan*, *75*, 180-186.

Franz, K. J., et al. (2008), Operational snow modeling: Addressing the challenges of an energy balance model for National Weather Service forecasts, *Journal of Hydrology*, *360*(1-4), 48-66.

Gabet, E. J., D. W. Burbank, J. K. Putkonen, B. A. Pratt-Sitaula, and T. Ojha (2004), Rainfall thresholds for landsliding in the Himalayas of Nepal, *Geomorphology*, *63*, 131-143.

Gadgil, S., et al. (2003), The Indian monsoon and its variability, *Annual Review of Earth and Planetary Sciences*, *31*(3), 429-467.

Galewsky, J. (2009), Rain shadow development during the growth of mountain ranges: An atmospheric dynamics perspective, *Journal of Geophysical Research-Earth Surface 114.*

Garbrecht, J., and L. W. Martz (1997), The Assignment of Drainage Direction over Flat Surfaces in Raster Digital Elevation Models, *Journal of Hydrology*, *193*, 204-213.

Gasse, F., et al. (1991), A 13,000-Year Climate Record from Western Tibet, *Nature*, *353*(6346), 742-745.

GDCNV1 (2002), Global Daily Climatology Network (GDCN), V1.0, National Climatic Data Center (released July 2002), accessible at http://www.ncdc.noaa.gov/oa/climate/research/gdcn/gdcn.html.

Guntner, A., et al. (2007), A global analysis of temporal and spatial variations in continental water storage, *Water Resources Research*, *43*(5).

Hahn, D. G., and S. Manabe (1975), Role of Mountains in South Asian Monsoon Circulation, *Journal of the Atmospheric Sciences*, *32*(8), 1515-1541.

Hall, D. K., et al. (2002), MODIS snow-cover products,

Remote Sensing of Environment(83), 181-194.

Hall, D. K., and K. A. Casey (2003), The MODIS Snow/Ice Global Mapping Project, *http://modis-snow-ice.gsfc.nasa.gov/modis.html*.

Harper, J. T., and N. F. Humphrey (2003), High altitude Himalayan climate inferred from glacial ice flux, *Geophysical Research Letters*, *30*(14).

Hasnain, S. I. (1999), Runoff characteristics of a glacierized catchment, Garhwal Himalaya, India, *Hydrological Sciences Journal-Journal Des Sciences Hydrologiques*, *44*(6), 847-854.

Hatwar, H. R., et al. (2005), Prediction of western disturbances and associated weather over Western Himalayas, *Current Science*, *88*(6), 913-920.

Herzschuh, U. (2006), Palaeo-moisture evolution in monsoonal Central Asia during the last 50,000 years, *Quaternary Science Reviews*, *25*(1-2), 163-178.

Hock, R. (2003), Temperature index melt modelling in mountain areas, *Journal of Hydrology*, *282*(1-4), 104-115.

Hollinger, J. P. (1990), Special Issue on the Defense Meteorological Satellite Program (DMSP - Calibration and Validation of the Special Sensor Microwave Imager (SSM/I), *Ieee Transactions on Geoscience and Remote Sensing*, *28*(5), 779-780.

Houze, R. A., D. C. Wilton, et al. (2007), Monsoon convection in the Himalayan region as seen by the TRMM Precipitation Radar, *Quarterly Journal of the Royal Meteorological Society, 133*, 1389-1411.

Huffman, G. J., et al. (2007), The TRMM multisatellite precipitation analysis (TMPA): Quasi-global, multiyear, combined-sensor precipitation estimates at fine scales, *Journal of Hydrometeorology*, *8*(1), 38-55.

Iguchi, T., et al. (2000), Rain-profiling algorithm for the TRMM precipitation radar, *Journal of Applied Meteorology*, *39*(12), 2038-2052.

Immerzeel, W. W., et al. (2009), Large-scale monitoring of snow cover and runoff simulation in Himalayan river basins using remote sensing, *Remote Sensing of Environment*, *113*(1), 40-49.

Ives, J. D., and B. Messerli (1989), *The Himalayan Dilemma: Reconciling Development and Conservation*, John Wiley and Sons, London, U.K.

Kozu, T., et al. (2001), Development of precipitation radar onboard the Tropical Rainfall Measuring Mission (TRMM) satellite, *Ieee Transactions on Geoscience and Remote Sensing*, *39*(1), 102-116.

Kumar, L., et al. (1997), Modelling topographic variation in solar radiation in a GIS environment, *International Journal of Geographical Information Science*, *11*(5), 475-497.

Kummerow, C., et al. (1998), The Tropical Rainfall Measuring Mission (TRMM) Sensor Package, *Journal of Atmospheric and Oceanic Technology*, *15*, 809-817.

Kummerow, C., et al. (2000), The status of the Tropical Rainfall Measuring Mission (TRMM) after two years in orbit, *Journal of Applied Meteorology*, *39*(12), 1965-1982.

Kundzewicz, Z. W., et al. (2007), Freshwater resources and their management, in *Climate Change 2007: Impacts, Adaptation and Vulnerability. Contribution of Working Group II to the Fourth Assessment Report of the Intergovernmental Panel on Climate Change*, edited by M. L. Parry, et al., pp. 173-210, Cambridge University Press, Cambridge, UK.

Lague, D., et al. (2005), Discharge, discharge variability, and the bedrock channel profile, *Journal of Geophysical Research-Earth Surface*, *110*(F4).

Lang, T. J., and A. P. Barros (2002), An investigation of the onsets of the 1999 and 2000 monsoons in central Nepal, *Mon. Weather Rev.*, *130*(5), 1299-1316.

Lang, T. J., and A. P. Barros (2004), Winter storms in the central Himalayas, *Journal of the Meteorological Society of Japan*, *82*(3), 829-844.

Lemke, P., et al. (2007), *Observations: Changes in Snow, Ice and Frozen Ground*, Cambridge University Press, Cambridge, United Kingdom and New York, NY, USA.

Linsley, R. K., Jr. (1943), A Simple Procedure for the daily forecasting of runoff from snowmelt, paper presented at Transaction of the American Geophysical Union, Part III, 62-67.

Magagi, R., and A. P. Barros (2004), Estimation of latent heating of rainfall during the onset of the Indian monsoon using TRMM PR and radiosonde data, *Journal of Applied Meteorology*, *43*(2), 328-349.

Martinec, J., et al. (2007), *Snowmelt runoff model (SRM): User's manual*, 175 pp., New Mexico State University, Las Cruces, New Mexcio.

Monteith, J. L. (1964), Evaporation and environment. The state and movement of water in living organisms, *Symposium of the society of experimental biology*, *Vol. 19*, 205-234, Cambridge: Cambridge University Press.

Mu, Q., F. A. Heinsch, M. Zhao, and S. W. Running (2007), Development of a global evapotranspiration algorithm based on MODIS and global meteorology data, *Remote Sensing of Environment*, *111*(4), 519-536.

Nash, J.E. and Sutcliffe, J.V. (1970), River flow forecasting through conceptual models part I – A discussion of principles, *Journal of Hydrology*, 10(3), 282-290.

Nesbitt, S. W., and A. M. Anders (2009), Very high resolution precipitation climatologies from the Tropical Rainfall Measuring Mission precipitation radar, *Geophysical Research Letters*, *36*.

Nijssen, B., and D. P. Lettenmaier (2004), Effect of precipitation sampling error on simulated hydrological fluxes and states: Anticipating the Global Precipitation Measurement satellites, *Journal of Geophysical Research-Atmosheres*, *109*(D2).

Parthasarathy, B., et al. (1992), Indian-Summer Monsoon Rainfall Indexes - 1871-1990, *Meteorological Magazine*, *121*(1441), 174-186.

Petersen, W. A., and S. A. Rutledge (2001), Regional variability in tropical convection: Observations from TRMM, *Journal of Climate*, *14*(17), 3566-3586.

Pratt, B., et al. (2002), Impulsive alluviation during early Holocene strengthened monsoons, central Nepal Himalaya, *Geology*, *30*(10), 911-914.

Putkonen, J. (2004), Continuous snow and rain data at 500 to 4400 m altitude near Annapurna, Nepal, 1999-2001, *Arctic, Antarctic, and Alpine Research*, *36*, 244-248.

Rango, A., and J. Martinec (1995), Revisiting the Degree-Day Method for Snowmelt Computations, *Water Resources Bulletin*, *31*(4), 657-669.

Rao, S. V. N., et al. (1996), A simple monthly runoff model for snow dominated catchments in western Himalayas, *Nordic Hydrology*, *27*(4), 255-274.

Riehl, H. (1959), On production of kinetic energy from condensation heating, in *The Atmosphere and the Sea in Motion*, edited, pp. 381-399, The Rockefeller Institute Press, The Rossby Memorial Volume, New York.

Sharma, P. D., A. K. Goel, and R. S. Minhas (1991), Water and Sediment Yields into the Sutlej River from the High Himalaya, *Mountain Research and Development*, *11*(2), 87-100.

Singh, P., S. K. Jain, and N. Kumar (1997), Estimation of snow and glacier-melt contribution to the Chenab River, Western Himalaya, *Mountain Research and Development*, *17*(1), 49-56.

Singh, P., and N. Kumar (1997), Impact assessment of climate change on the hydrological response of a snow and glacier melt runoff dominated Himalayan river, *Journal of Hydrology*, *193*(1-4), 316-350.

Singh, P., and M. C. Quick (1993), Streamflow Simulation of Satluj River in the Western Himalaya, *Snow and Glacier Hydrology*, *218*, 261-271.

Smith, R. B., and J. P. Evans (2007), Orographic precipitation and water vapor fractionation over the southern Andes, *Journal of Hydrometeorology*, *8*(1), 3-19.

Smith, R. B., and I. Barstad (2004), A linear theory of orographic precipitation, *Journal of the Atmospheric Sciences*, *61*(12), 1377-1391.

Snyder, N. P., et al. (2003), Importance of a stochastic distribution of floods and erosion thresholds in the bedrock river incision problem, *Journal of Geophysical Research-Solid Earth*, *108*(B2).

Staubwasser, M., et al. (2002), South Asian monsoon climate change and radiocarbon in the Arabian Sea during early and middle Holocene, *Paleoceanography*, *17*(4).

Steiner, M., et al. (2003), Comparison of two methods for estimating the sampling-related uncertainty of satellite rainfall averages based on a large radar dataset, *Journal of Climate*, *16*(22), 3759-3778.

Sun, Z. G., Q. X. Wang, Z. Ouyang, M. Watanabe, B. Matsushita, and T. Fukushima (2007), Evaluation of MOD16 algorithm using MODIS and ground observational data in winter wheat field in North China Plain, *Hydrological Processes*, *21*(9), 1196-1206.

Tarboton D. G., R. L. Bras, I. Rodriguez-Iturbe (1991), On the Extraction of Channel Networks from Digital Elevation Data, Hydrological Processes, 5, 81-100

Viviroli, D., et al. (2007), Mountains of the world, water towers for humanity: Typology, mapping, and global significance, *Water Resources Research*, *43*(7).

Wan, Z., and J. Dozier (1996), A generalized split-window algorithm for retrieving land-surface temperature from space, *Ieee Transactions on Geoscience and Remote Sensing*, *34*(4), 892-905.

Wan, Z., et al. (2004), Quality assessment and validation of the MODIS global land surface temperature, *International Journal of Remote Sensing*, *25*(1), 261-274.

Wan, Z. M., et al. (2002), Validation of the land-surface temperature products retrieved from Terra Moderate Resolution Imaging Spectroradiometer data, *Remote Sensing of Environment*, *83*(1-2), 163-180.

Wan, Z. M. (2008), New refinements and validation of the MODIS Land-Surface Temperature/Emissivity products, *Remote Sensing of Environment*, *112*(1), 59-74.

Wang, B. (2006), *The Asian Monsoon*, 787 pp., Springer, Berlin.

Webster, P. J. (1983), Mechanisms of Monsoon Low-Frequency Variability - Surface Hydrological Effects, *Journal of the Atmospheric Sciences*, *40*(9), 2110-2124.

Webster, P. J. (1987), *The Elementary Monsoon*, 3-32 pp., Wiley, New York.

Webster, P. J., et al. (1998), Monsoons: Processes, predictability, and the prospects for prediction, *Journal of Geophysical Research-Oceans*, *103*(C7), 14451-14510.

Whipple, K. X. (2004), Bedrock rivers and the geomorphology of active orogens, *Annual Review of Earth and Planetary Sciences*, *32*, 151-185.

Wulf, H., Bookhagen, B. and Scherler, D. (2010), Seasonal precipitation gradients and their impact on erosion in the Northwest Himalaya, *Geomorphology,* doi:10.1016/j.geomorph.2009.12.003

Towards a complete Himalayan hydrologic budget: The spatiotemporal distribution of snowmelt and rainfall and their impact on river discharge by B. Bookhagen and D. Burbank
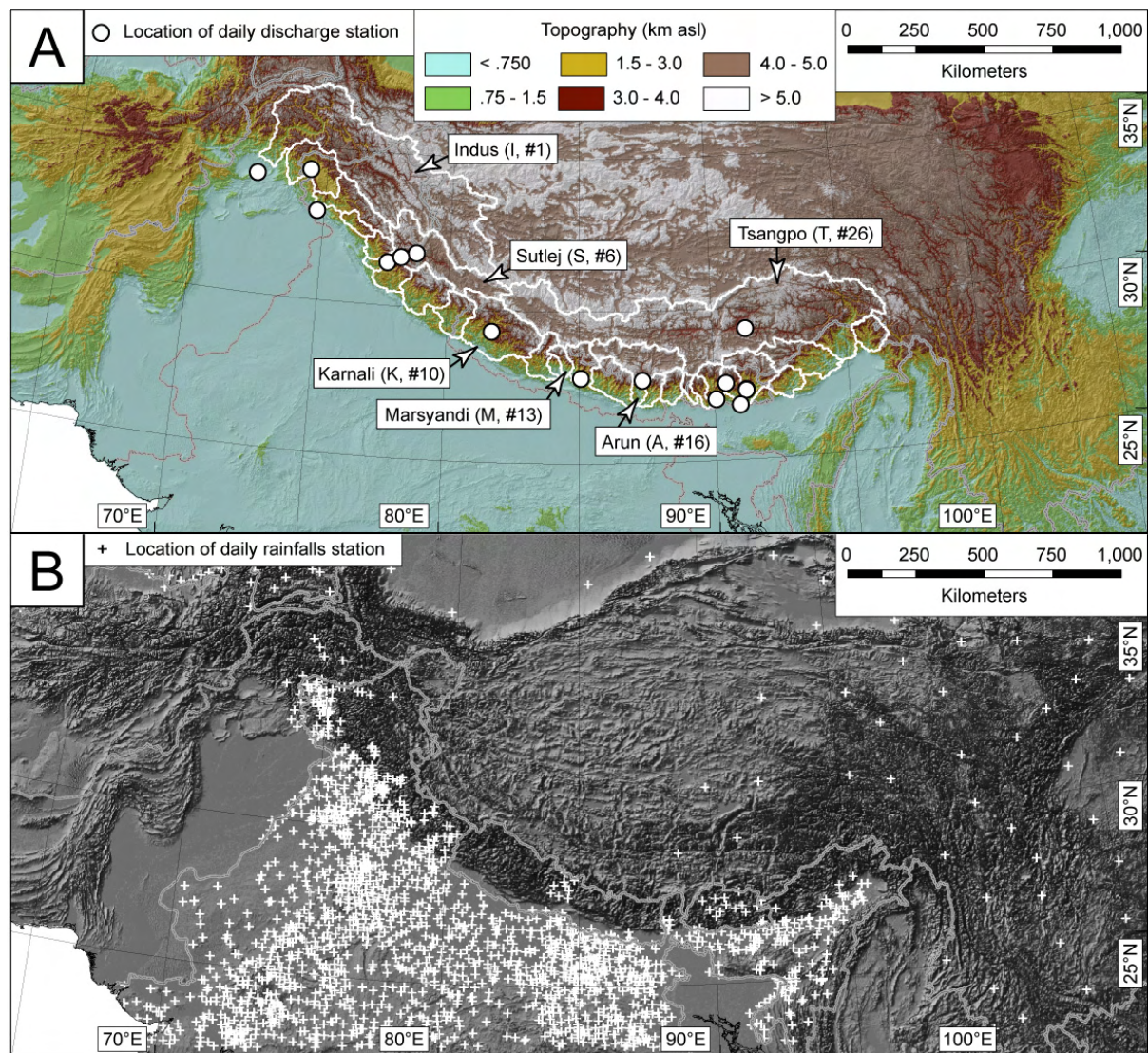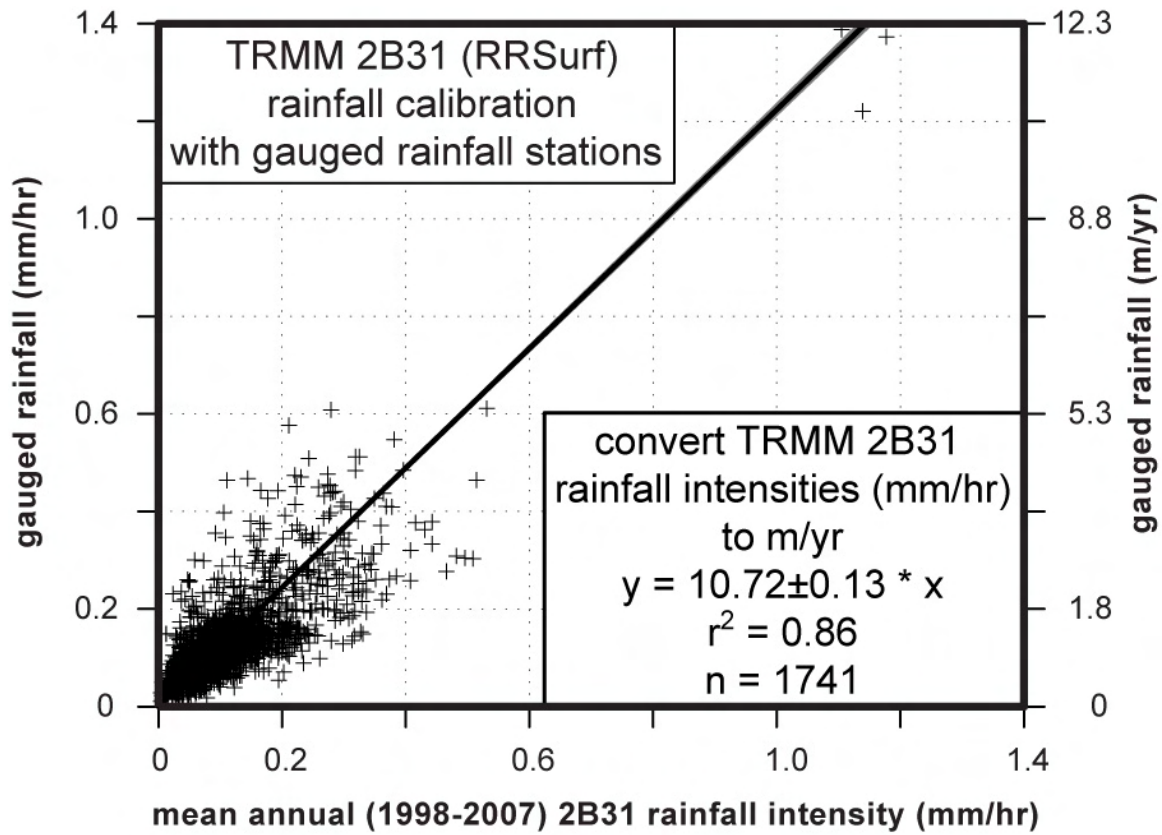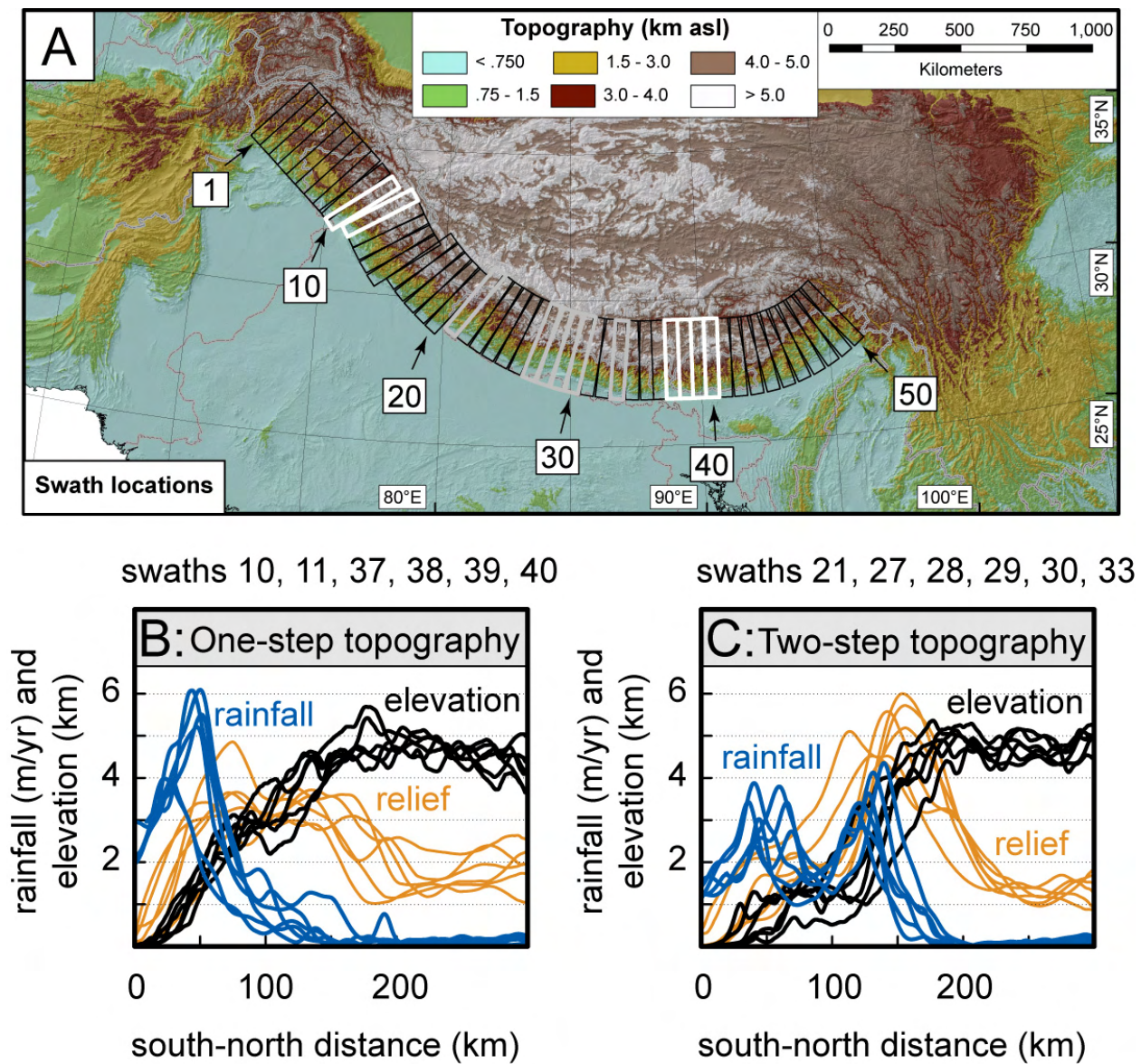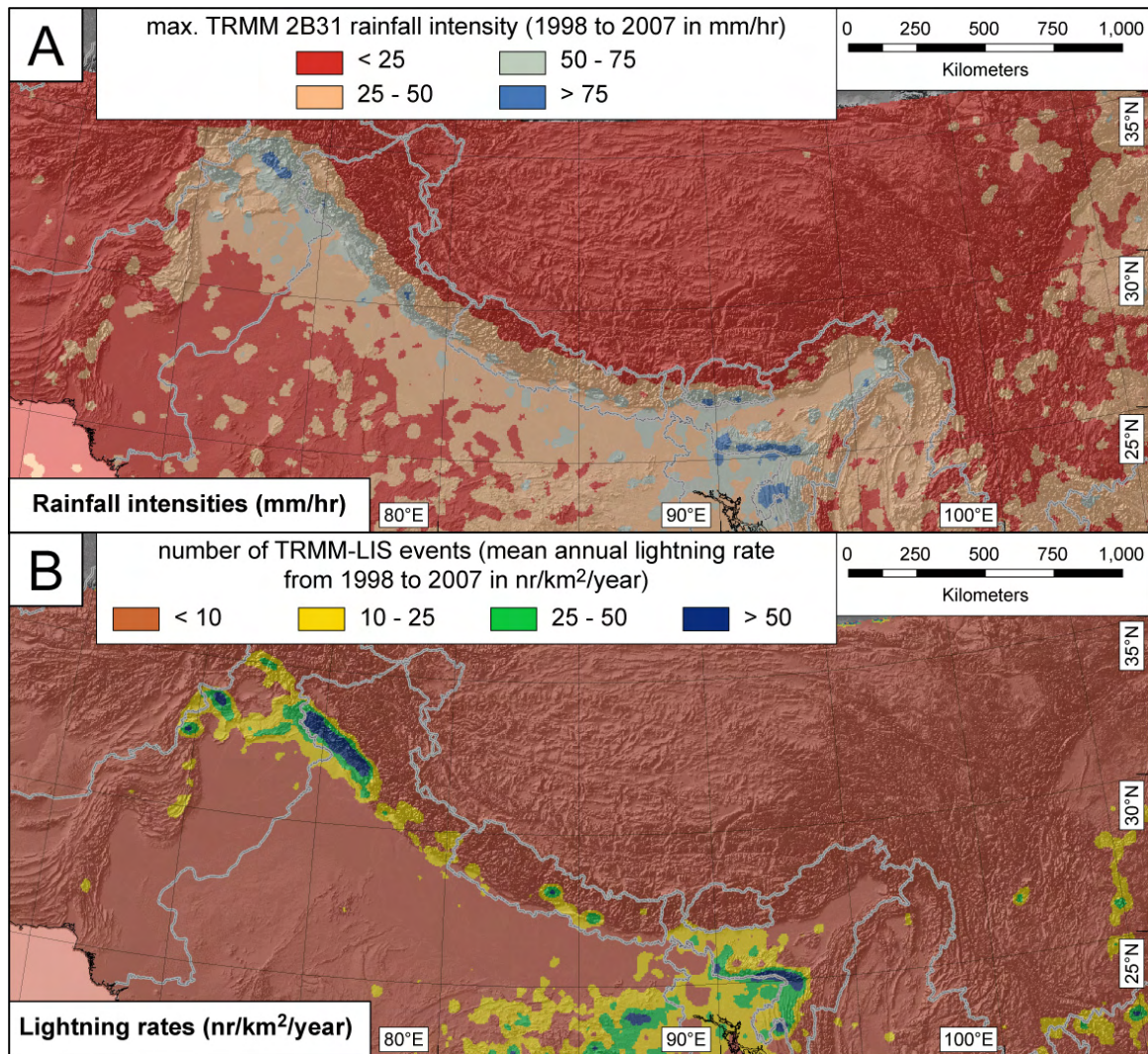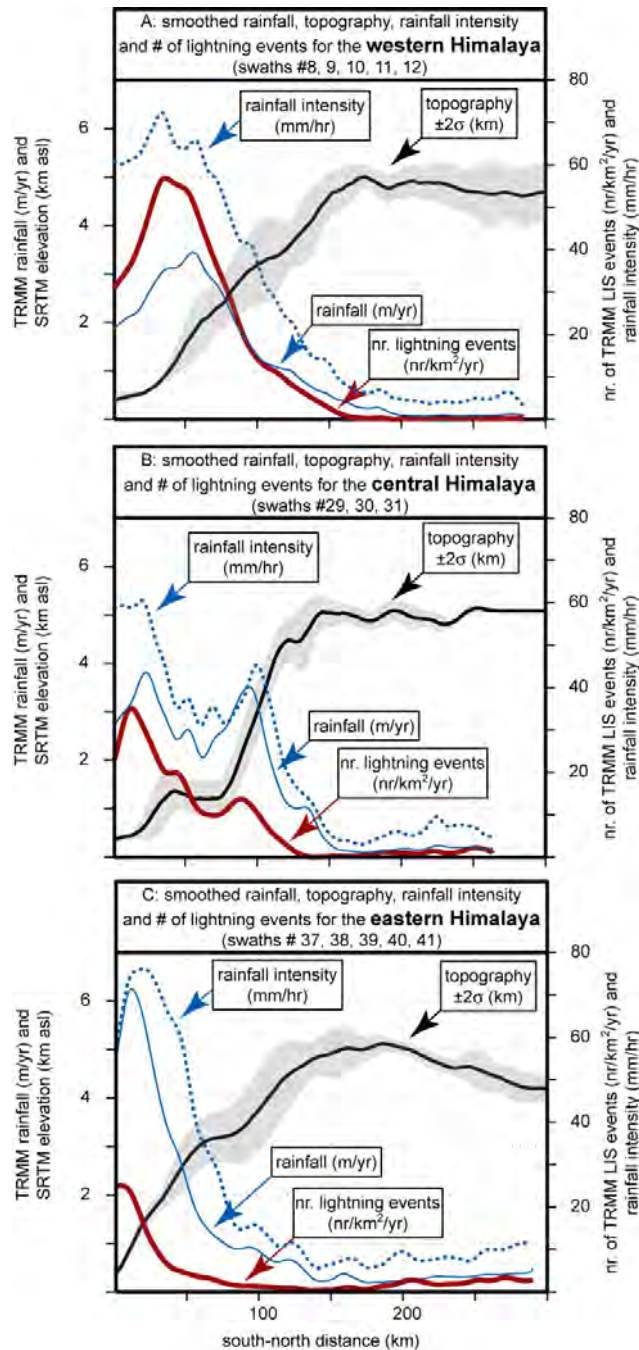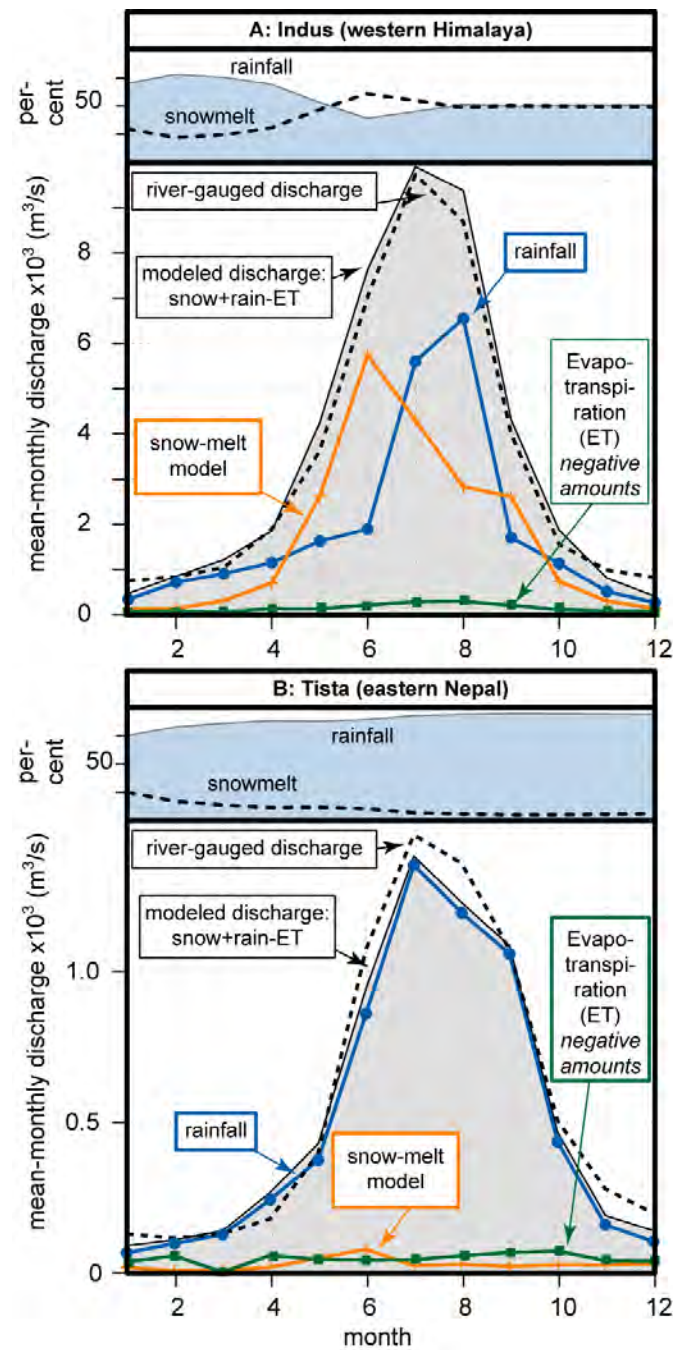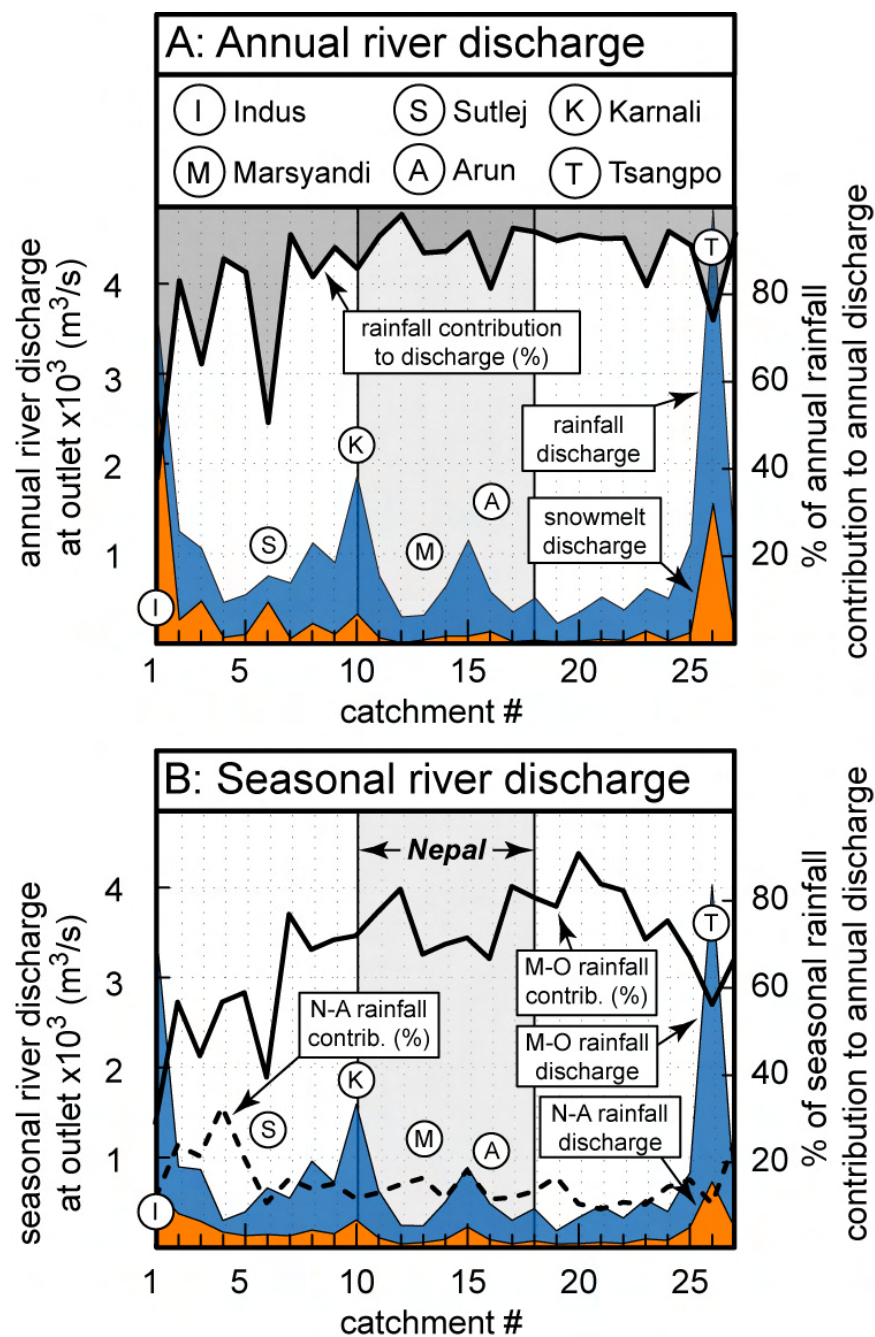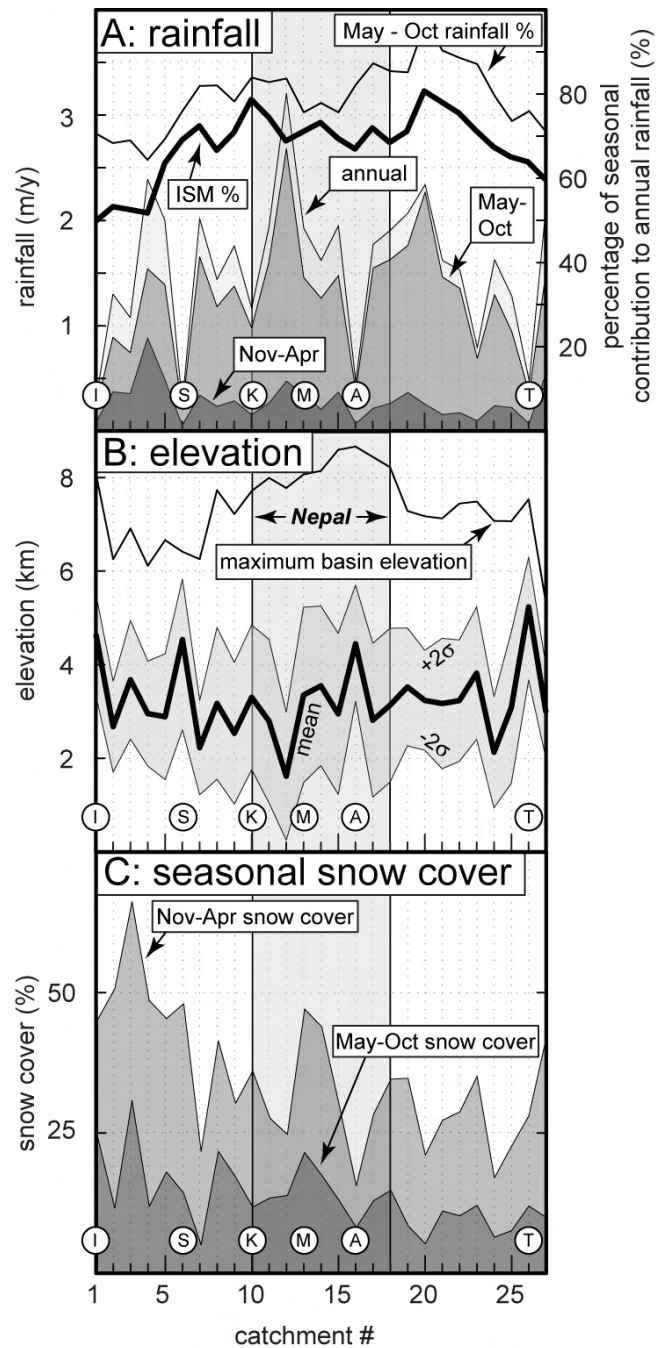

Figure 1

Figure 2
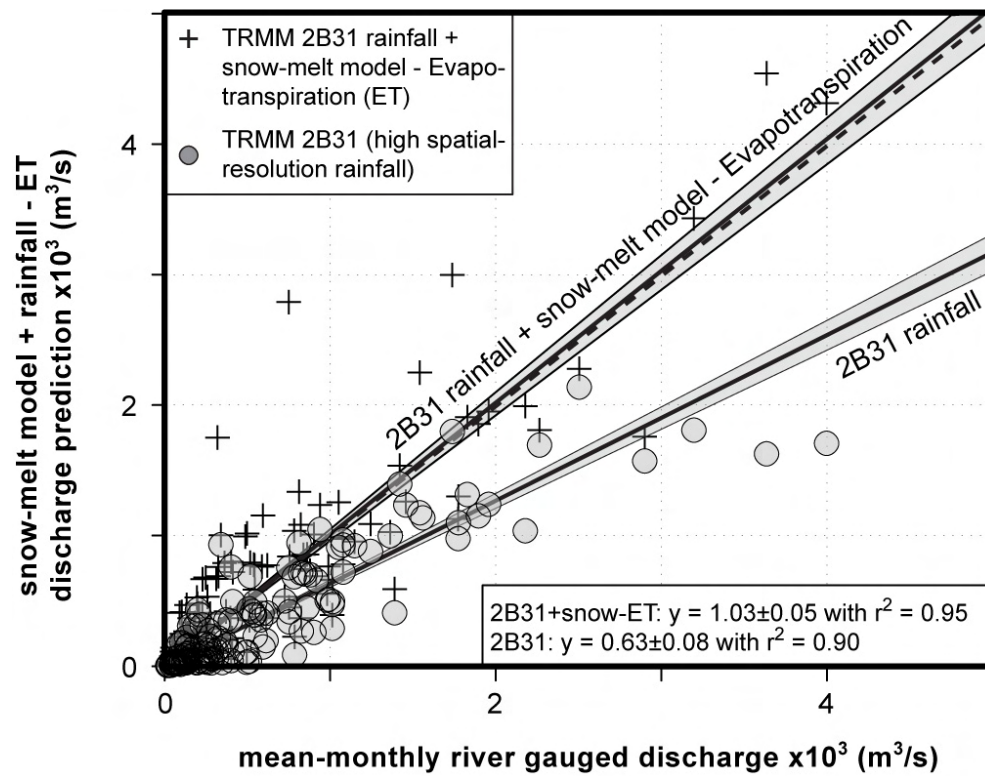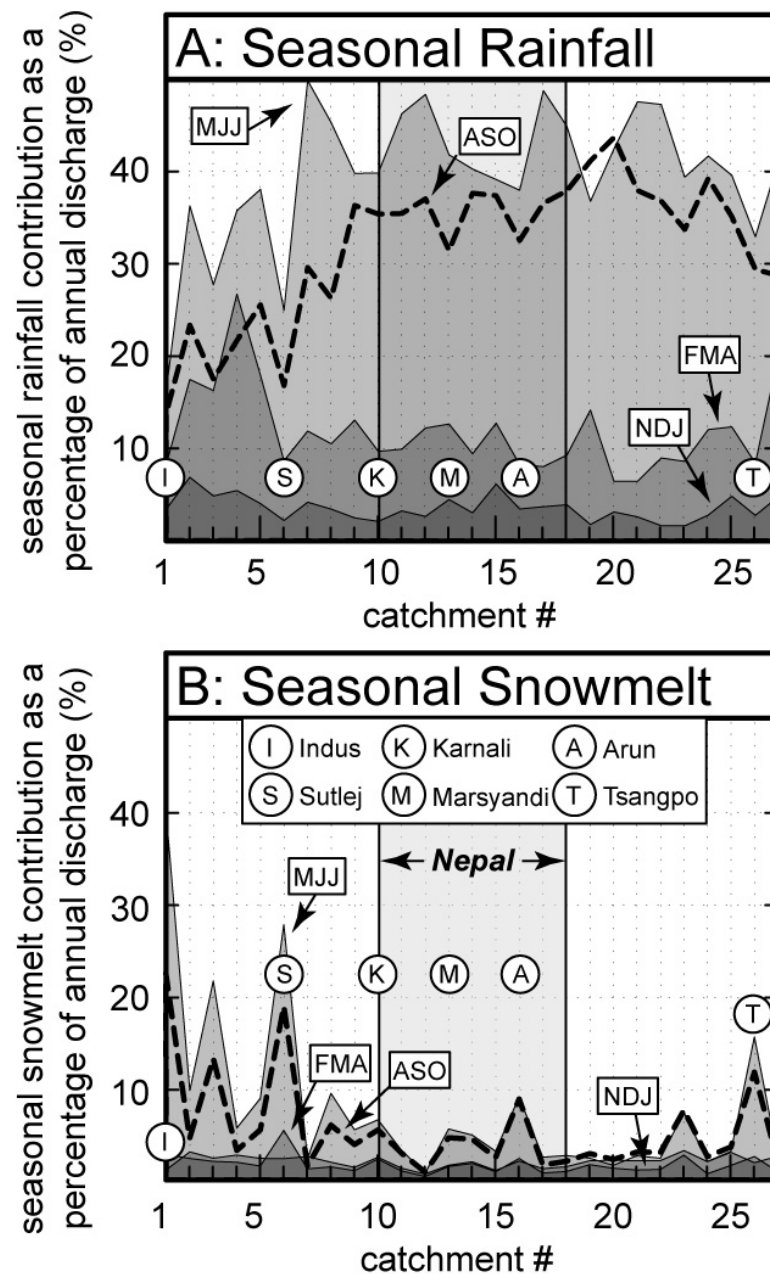
Figure 3
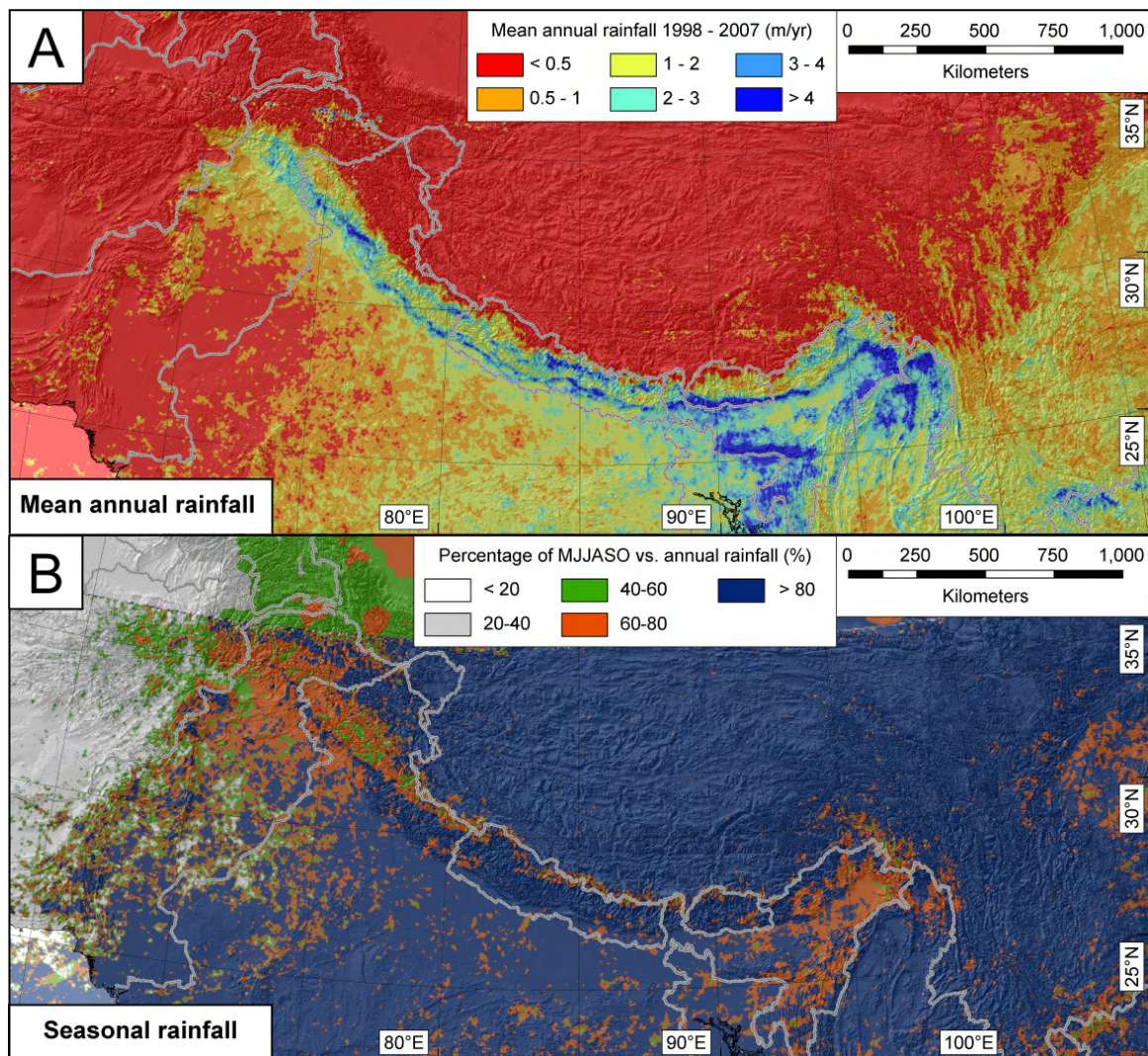
Figure 4
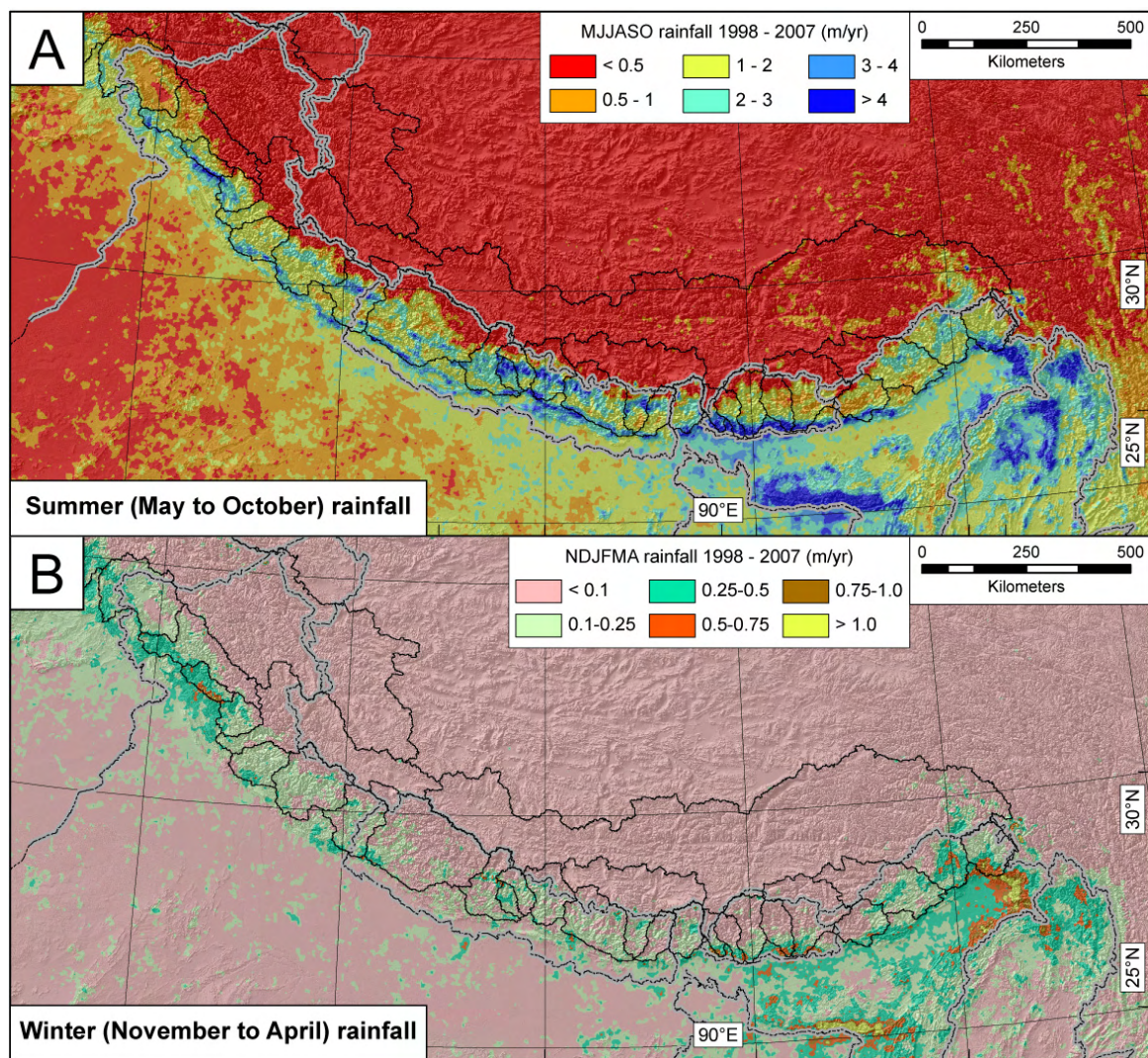
Figure 5
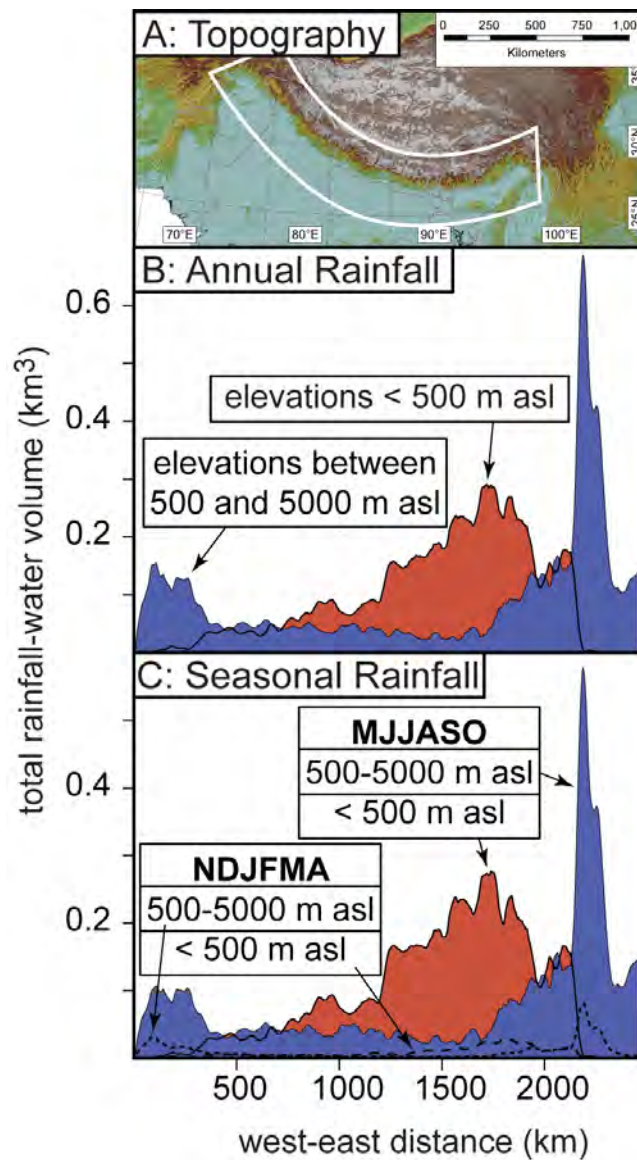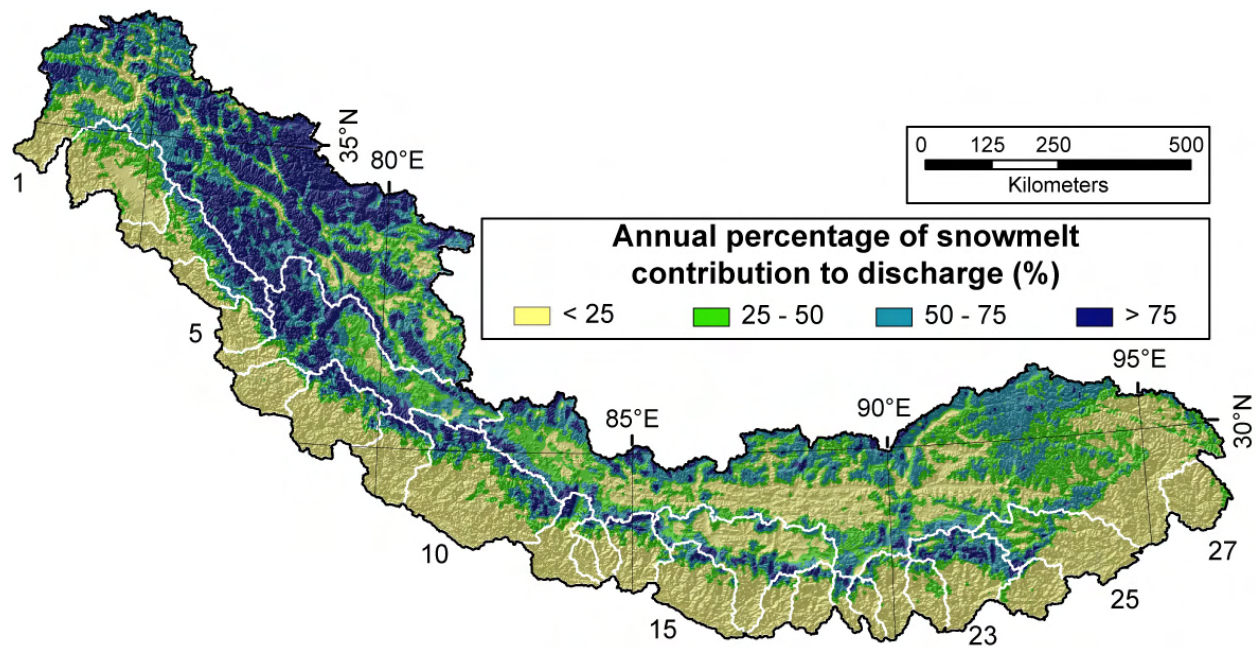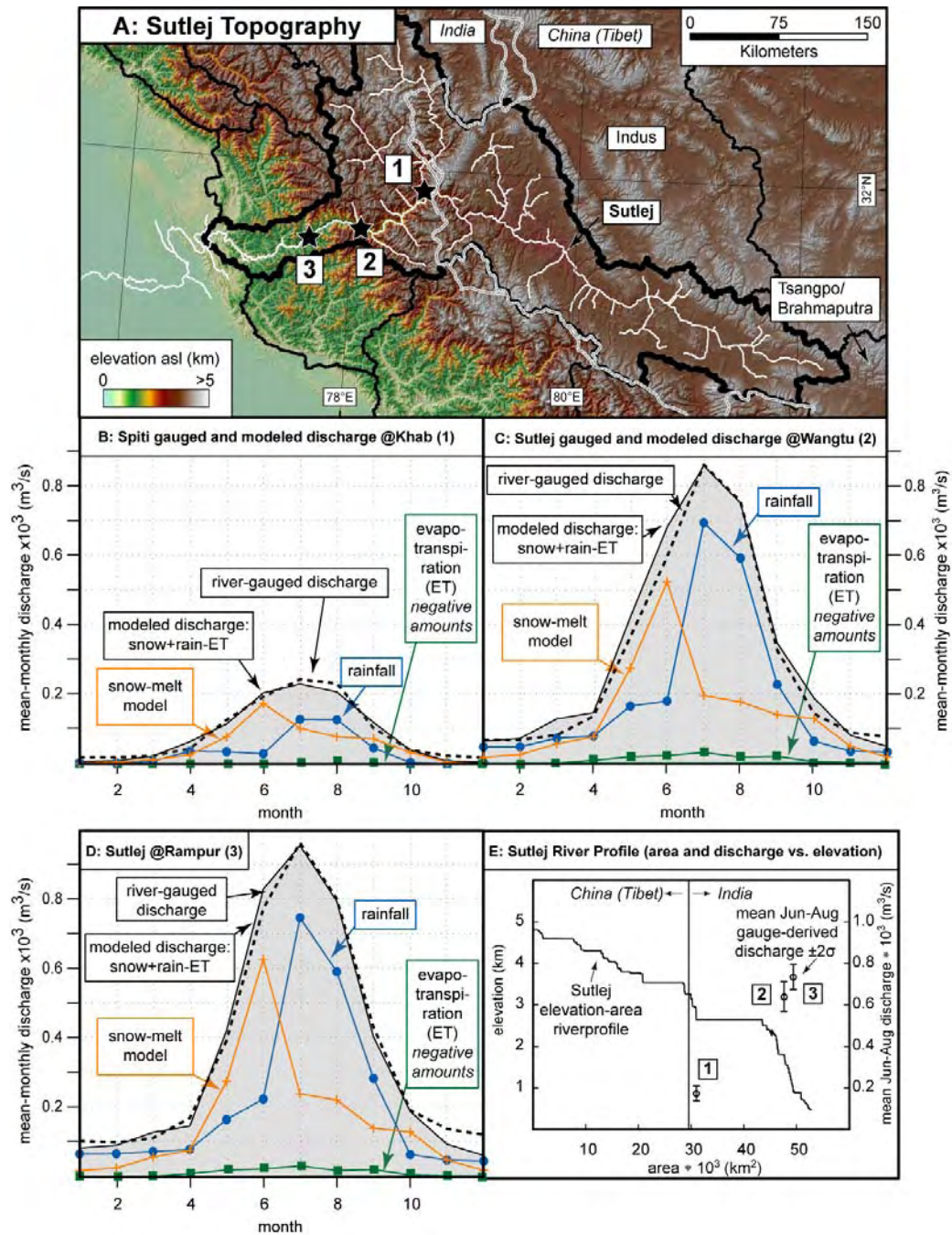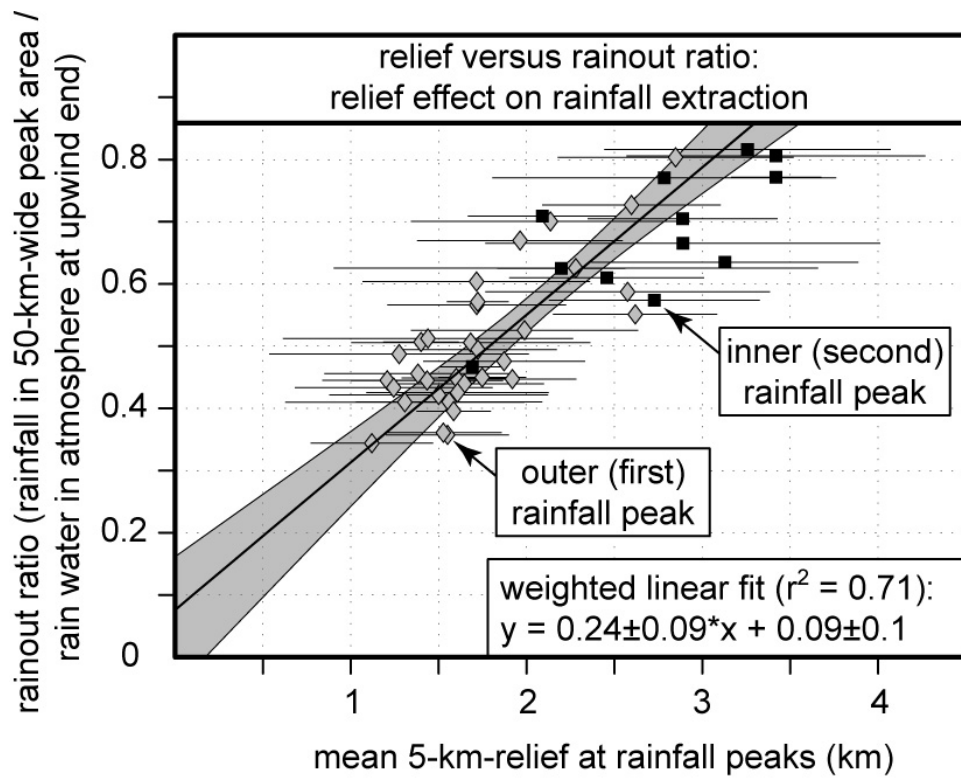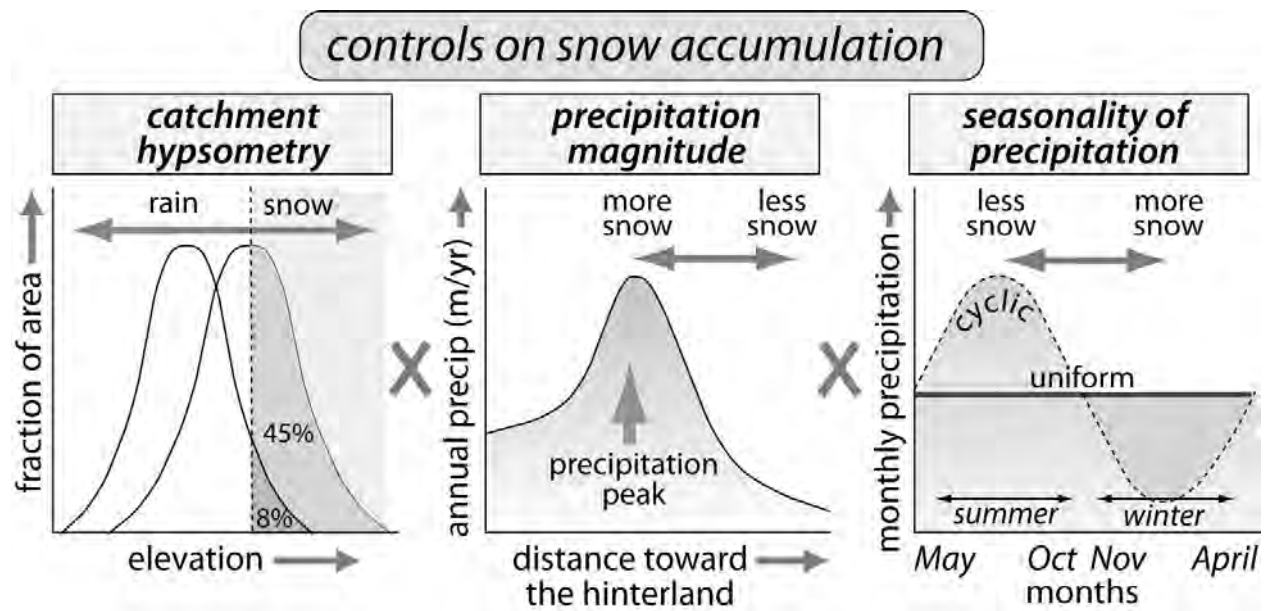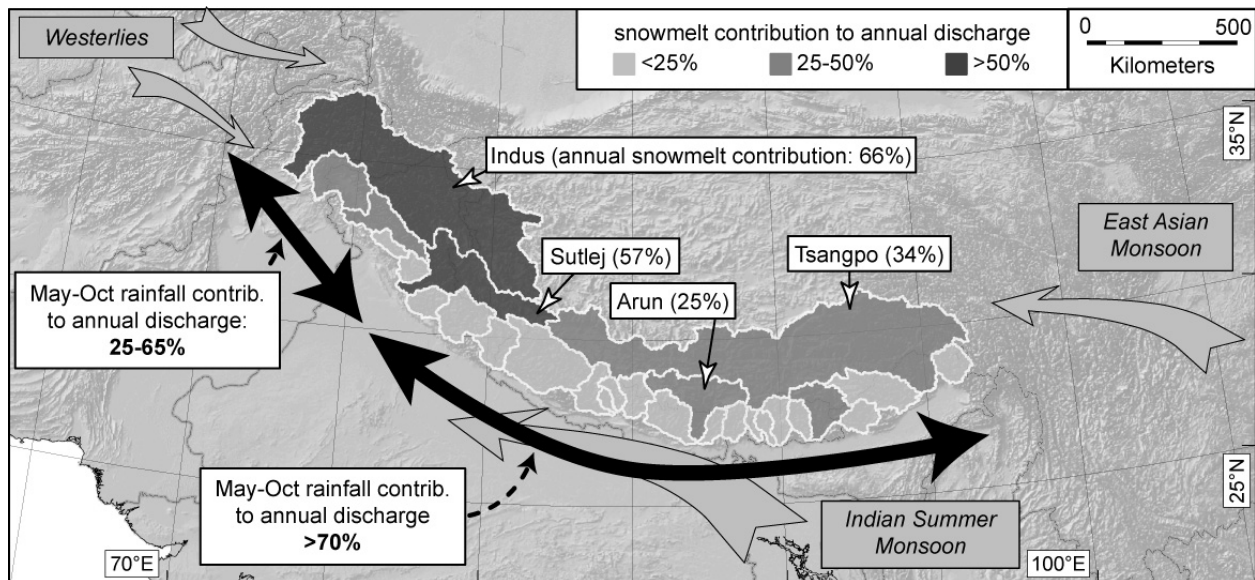
Figure 6

Figure 7

Figure 8

Figure 9

Figure 10

Figure 11

11

Figure 12

Towards a complete Himalayan hydrologic budget: The spatiotemporal distribution of snowmelt and rainfall and their impact on river discharge by B. Bookhagen and D. Burbank

Figure 13

Figure 14

Towards a complete Himalayan hydrologic budget: The spatiotemporal distribution of snowmelt and rainfall and their impact on river discharge by B. Bookhagen and D. Burbank

Figure 15

Figure 16

Figure 17

Towards a complete Himalayan hydrologic budget: The spatiotemporal distribution of snowmelt and rainfall and their impact on river discharge by B. Bookhagen and D. Burbank

Figure 18

Towards a complete Himalayan hydrologic budget: The spatiotemporal distribution of snowmelt and rainfall and their impact on river discharge

Bodo Bookhagen[1], Douglas W. Burbank[2]

1Geography Department, UC Santa Barbara, Santa Barbara, CA 93106, USA

2Institute for Crustal Studies, UC Santa Barbara, Santa Barbara, CA 93106, USA

Supplementary data

Data processing

1. Topographic data

Because the SRTM data are not continuous, we filled minor holes of a few pixels by interpolation and filled larger holes with 90-m elevation-adjusted Digital Terrain Elevation Data (DTED). For the remaining regions with missing topographic information, we used digital elevation models (DEMs) created from stereo-views of the Advanced Spaceborne Thermal Emission and Reflection Radiometer (ASTER).

2. Rainfall data

We used raw, orbital satellite data from the Tropical Rainfall Measurement Mission (TRMM) to estimate rainfall amounts [*Kummerow et al.*, 1998; *Kummerow et al.*, 2000]. The TRMM product 2B31provides rainfall estimates on a 4 x 6 km^2 pixel size between 36°N and 36°S. During processing, we interpolated every orbit onto an equally-spaced 5 x 5 km^2 grid. [Product 2B31, algorithm V6, more information are available at: http://disc.sci.gsfc.nasa.gov/precipitation/documentation/TRMM_README/TRMM_2B31_readme.shtml]. During the measurement period (1998-2007), the TRMM platform experienced a boost (Aug 24th, 2001) to extend the platform's lifetime. This changed the horizontal resolution at the Earth's surface from 4.3 to ~5 km. Our bilinear interpolation scheme re-projects the measurements from its orbital coordinates to an equally-spaced grid on the Earth surface (latitude/longitude grid). TRMM 2B31 data is a combined rainfall profile product from the Precipitation Radar (PR) and TRMM Microwave Imager (TMI). The TMI is a nine-channel passive microwave radiometer, which builds on the heritage of the Special Sensor Microwave/Imager (SSM/I) instrument [*Bookhagen et al.*, 2005a; *Hollinger*, 1990]. The Precipitation Radar (PR), the first of its kind in space, is an

electronically scanning radar operating at 13.8 GHz that measures the 3-D rainfall distribution over both land and ocean. The combined 2B31 algorithm uses the low-frequency channels of TMI to find the total path attenuation. This attenuation is used to constrain the radar equation to estimate the surface rain rate in mm/hr. We use root-mean square uncertainties of the surface-rainfall rate of each measurement to estimate the errors associated with each grid cell.

The TRMM algorithms that have been used for deriving rainfall amounts are interpreted to primarily represent rainfall amounts and do not include snowfall amounts. Remote sensing of snowfall is a difficult process, as snowflakes (or frozen precipitation) have different sizes, shapes, and densities resulting in complex radar echoes. In contrast, rain and raindrops consist of water, which has a known and fixed dielectric constant and thus is argued to interact with the radar wave in a predictable way. The sensors onboard the TRMM platform have been designed to sense tropical rainfall [*Kummerow et al.*, 1998]. However, on some of the higher peaks in the Karakoram (northern Pakistan) the TRMM algorithm predicts 4 m/yr rainfall at ~6 km elevation – a clearly unrealistic amount. Similarly, some of the high summits with persistent snow cover in the central Himalaya are associated with remotely-sensed rainfall amounts that are too high. We attribute this overestimation to potential scattering effects of snowfields. Although it is important to be aware of these discrepancies, the areas of the over-predicted rainfall amounts are only on the orders of several pixels and thus very small (< 100 km^2). They can safely be ignored on the spatial scales of catchments (3 to 250 x10^3 km^2) or entire mountain ranges on which we focus in this study.

We processed these data for 10 consecutive years from 1998 to 2007 with a total of 57,718 orbits (~16 each day). Because the orbital path of the TRMM satellite results in its own platform coordinate system, we bilinearly interpolated every orbit onto an equally-spaced 5 x 5 km^2 grid with a latitude/longitude reference frame on the Earth surface. The number of measurements (or observations) of the TRMM 2B31 data product depends on the number of overpassing orbits. This number, in turn, depends on the latitude: higher latitudes are observed more often, because the satellite's orbital path crosses them during the ascending and descending flights. In general, latitudes at ~35°N

have twice as many TRMM observations as the Himalayan foreland at ~28°N. In order to avoid overestimation of rainfall at higher latitudes, we explicitly correct for the time-dependent number of measurements as a function of latitude.

We have explicitly calculated the root mean square error for each measurement to account for satellite-derived uncertainties (Figure DR1). The combined (PR and TMI) product estimates errors by comparing predicted and measured brightness temperatures: large standard deviations imply that the measurements are too inconsistent with the physical model even after allowing for imperfections in the models and noise in the measurements. In contrast, small standard deviation indicate that the models can indeed explain the measurements if the parameters are given the values specific by the conditional means. Overall and throughout the Himalaya, our root mean square errors fit the physical model within 10% error (Figure DR1).
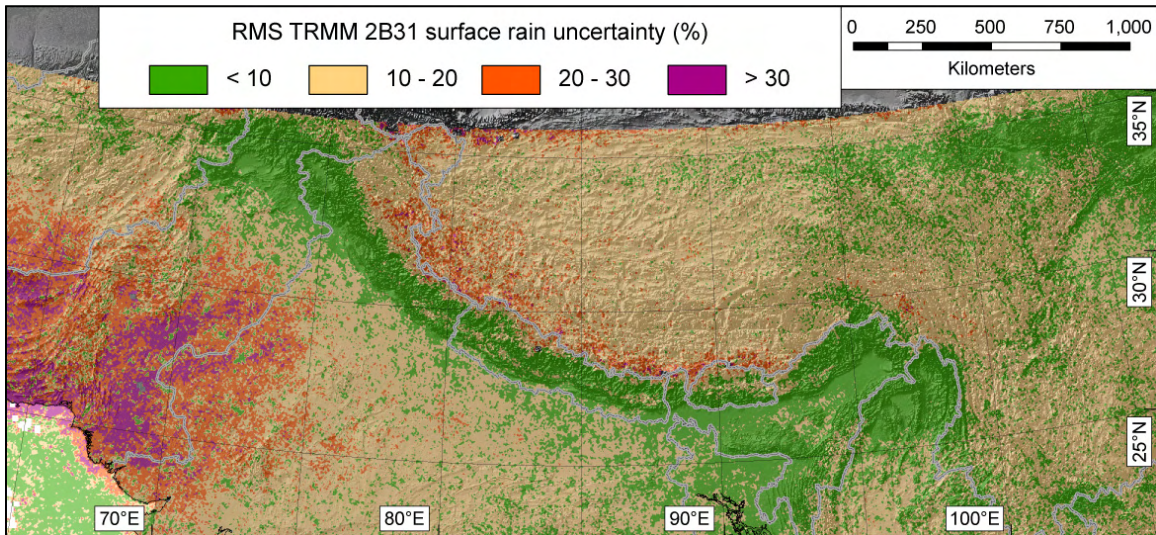
Figure DR1: Root-Mean-Square Errors of the surface rainfall (TRMM product 2B31) used in this study. We rely on satellite-retrieval errors (see text) and show the errors in percent compared to the absolute surface-rainfall amounts. Errors in our study area (Himalaya) are generally <10%, but are significantly larger in regions with lower rainfall amounts.

After scaling the data, the rainfall amounts were calibrated with daily, ground-based rainfall measurement from the mountainous areas of central Nepal and Bhutan (n = 19), and from the Indian subcontinent (n = 1722, see Figure 1 for location and Figure 2 to Figure 3 and Figure DR2 for calibrations) [*Barros et al.*, 2000; *Bookhagen and Burbank*,

2006; *GDCNV1*, 2002]. Generally, the data reveal robust and consistent results, even though the stations span >10° in latitudinal, >30° in longitudinal direction, and an elevation range from sea level to 4.5 km asl elevation (Figure DR2). Most of the heavy rainfall occurs below 4 km [*Barros et al.*, 2000; *Bookhagen and Burbank*, 2006; *Parthasarathy et al.*, 1992] and almost none above 6000 m [*Harper and Humphrey*, 2003]. We fitted the data using a robust least-squares method in which we minimize the summed square of the residuals and downweight outliers using bisquare weights. We have weighted the TRMM surface-rainfall rate with the root mean square estimates of the path attenuation fit. In order to derive a monthly rainfall dataset, we have calibrated mean monthly data averaged over the past 10 years using the same rain-gauge stations. We have removed unrealistically high rainfall intensities during orbit processing [*Iguchi et al.*, 2000; *Kozu et al.*, 2001]. Our calibration efforts and parameters match those from a similar study in the Andes of South America [*Bookhagen and Strecker*, 2008]. In general, the remotely-sensed rainfall data correlate very well with the ground-control stations: even high annual-rainfall amounts above 5 m/yr are accurately depicted (Figure 2 and Figure DR2). This corroborates our earlier findings from the Himalaya indicating that, despite non-continuous TRMM-rainfall data series, relative values represent a valid rainfall distribution [*Bookhagen and Burbank*, 2006].
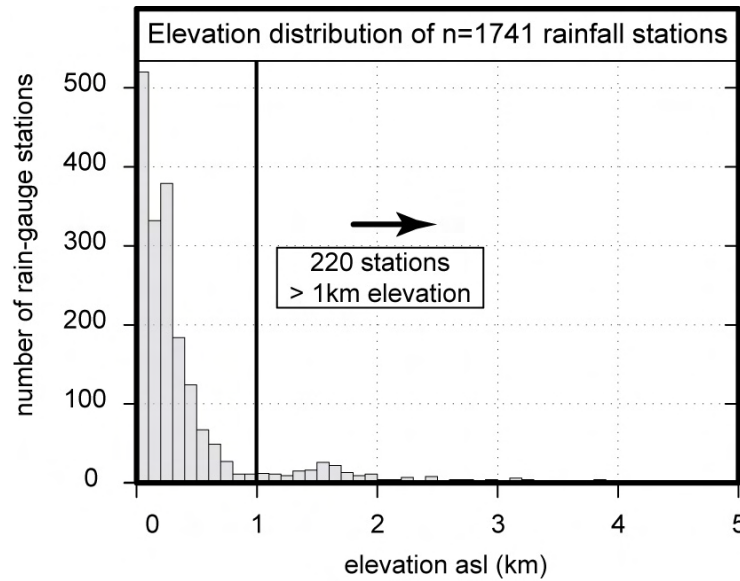
Figure DR2: Elevation histogram of rainfall stations (n=1741) used for calibration (see Figure 1B) for locations. The majority of the stations are from elevations below 1km, but there are more than 220 stations above 1km and more than a dozen stations above 3 km elevation.

Whereas the TRMM satellite captures most of the Himalaya, its orbital path does not include regions north of 36°N latitude. Thus, the northern parts of the Indus catchment are not covered by the high-resolution data. We, therefore, substituted these regions with the combined rainfall instrument calibration algorithm following 3B42, Version 6 [e.g., *Huffman et al.*, 2007; *Kummerow et al.*, 2000]. This algorithm uses an optimal combination of 2B31, 2A12, SSM/I (Special Sensor Microwave/Imager), AMSR (Advanced Microwave Scanning Radiometer), and AMSU (Advanced Microwave Sounding Unit) precipitation estimates. The output is gridded rainfall for 0.25x0.25 degree grid boxes (~30x30 km) on a 3-hour temporal resolution in a global belt extending from 50°S to 50°N. Although these data have a significantly lower spatial resolution, they provide rainfall estimates for the same time frame as the high-resolution TRMM product 2B31. The substituted part represents ~20% (~43 x 10^3 km^2) of the Indus catchment that has a total Himalayan drainage area of approximately 205 x 10^3 km^2. Because the substituted region lies in the high-elevation terrain with low annual rainfall amounts, use of a spatially lower-resolution dataset appears justified. In addition to patching the 2B31 dataset, we have created a mean-monthly time series of the 3B42 data.

We used both the high- (2B31) and low-spatial resolution (3B42) rainfall datasets to calculate the accumulated flow using the 90-m flow routing grid derived from the patched topographic data. We have routed the flow for every month, as well as an annual amount.
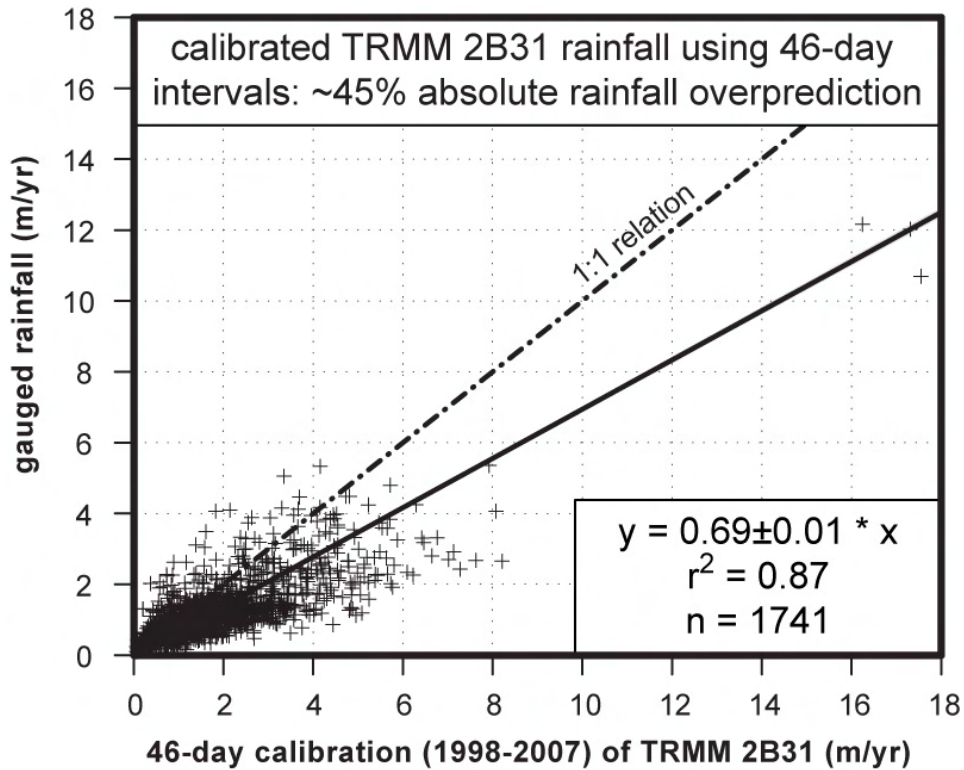
Figure DR3: Comparison of 46-day TRMM calibration (see text) with gauged rainfall (see Figure 1B for station locations). In this calibration routine, the year is divided into eight 46-day intervals – the period the TRMM satellites revisits a given location at the same time of day. Within this period, all measurements from different times of the day are averaged and multiplied by the length of the period. The relation with gauge rainfall is robust (r^2 = 0.87), but the 46-day calibration overpredicts rainfall by approximately 45%.

3. TRMM Lightning Image Sensor (LIS)

The Lightning Imaging Sensor (LIS) onboard the TRMM satellite consists of a staring imager, which is optimized to locate and detect lightning with storm-scale resolution (4 to 7 km) over a large region (~600 x 600 km) using a 128 x 128 charge coupled device (CCD) array [*Christian* et al., 1999]. We processed all available non-gridded, daily data between 1998 and 2006 (http://thunder.msfc.nasa.gov/data). The TRMM satellite travels a distance of 7 kilometers every second as it orbits the Earth, thus allowing the LIS to observe a point on the Earth or a cloud for almost 90 seconds as it passes overhead. Despite the brief duration of an observation, it is long enough to estimate the flashing rate of most storms. The LIS sensor records the time of occurrence, measures the radiant energy, and determines the location of lightning events within its field-of-view.

6

4. Snow-cover area, surface temperature, and solar radiation

We have used the MOD10C2 product, which is part of the MODIS snow products [*Hall et al.*, 2002; *Hall and Casey*, 2003]. The automated MODIS snow-mapping algorithm uses at-satellite reflectance in MODIS bands 4 (0.545-0.565 mm) and 6 (1.628-1.652 mm) to calculate the normalized difference snow index (NDSI) [*Hall et al.*, 2002]. A pixel in a non-densely forested region will be mapped as snow if the NDSI is ≥0.4 and reflectance in MODIS band 2 (0.841 – 0.876 mm) is >11%. However, if the MODIS band 4 reflectances is <10%, the pixel will not be mapped as snow even if the other criteria are met. There are some difficulties accurately identifying dense snow cover in vegetated areas [*Hall et al.*, 2002], but vegetation cover in the higher-elevated Himalaya, where most of the snow falls, is negligible.

In order to estimate land surface temperature, we have used the MODIS Land Surface Temperature (LST) product MOD11C, which has similar spatial and temporal characteristics as the MOD10C2 product [*Wan et al.*, 2004]. A variety of LST methods have been used and published – the MOD11 product relies on a split-window method that requires known surface emissivities to make correction for the atmospheric and surface emissivity effects based on the differential atmospheric absorption in the 10-13 mm split window [*Wan and Dozier*, 1996; *Wan et al.*, 2002]. This product retrieves surface spectral emissivities and temperatures from a pair of daytime and nighttime MODIS data, therefore generating a minimum and maximum temperature range. We have used an optimized and refined MODIS surface temperature product that estimates temperatures with a root mean square difference of less than 0.7°K [*Wan*, 2008]. These data are then used to calculate the days with a mean temperature above freezing.
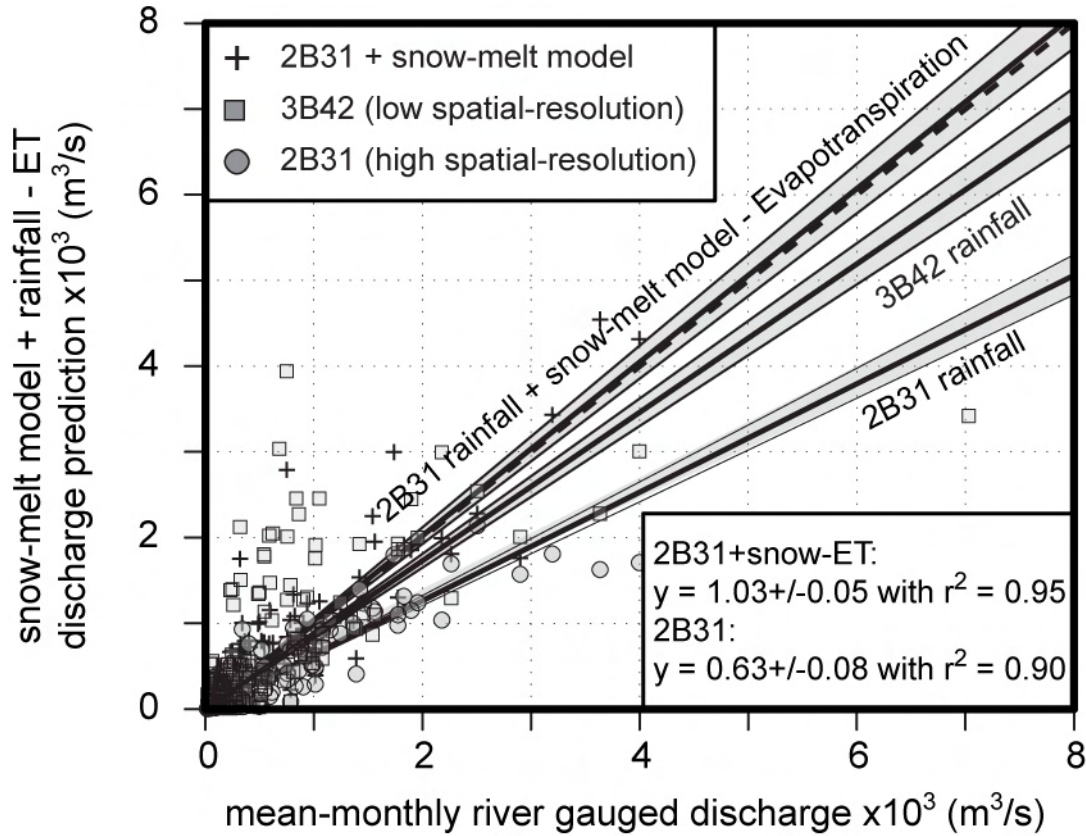
Figure DR4: Validation results of discharges derived from rainfall (2B31 and 3B42, snowmelt model and evapotranspiration. This figure is similar to Figure 4, but it includes results from the 3B42 climatology. We have used 13 stations (n = 12x13 = 156) that recorded daily discharge amounts during out modeling period (2000 to 2007) through the Himalaya. The bold dashed line indicates a 1:1 relation. The runoff from the TRMM3B42 rainfall is close to the measured discharge amounts and significantly higher than the TRMM2B31 rainfall. This is explained by the generally higher rainfall amounts over a larger area of the 3B42 dataset that result in higher discharge amounts, but overestimate grid-cell rainfall.

5. Evapotranspiration

The evapotranspiration (ET) amounts were derived from MODIS product MOD16 as described in *Cleugh et al.* [2007], *Mu et al.* [2007] and *Sun et al.* [2007]. This algorithm is based on the Penman-Monteith method and considers both the surface energy partitioning process and environmental constraints on ET [*Monteith*, 1964; *Cleugh et al.*, 2007]. The improved algorithm developed by *Mu et al.* [2007] was evaluated with 19 AmeriFlux eddy covariance flux towers and shows a robust ($r^2 = 0.76$) correlation with the field data.

In this study, the daily data were summed up per month and then averaged over a 7-year period to obtain mean monthly values. Similarly, the annual amounts were derived for each year before an average was calculated (Figure DR4).
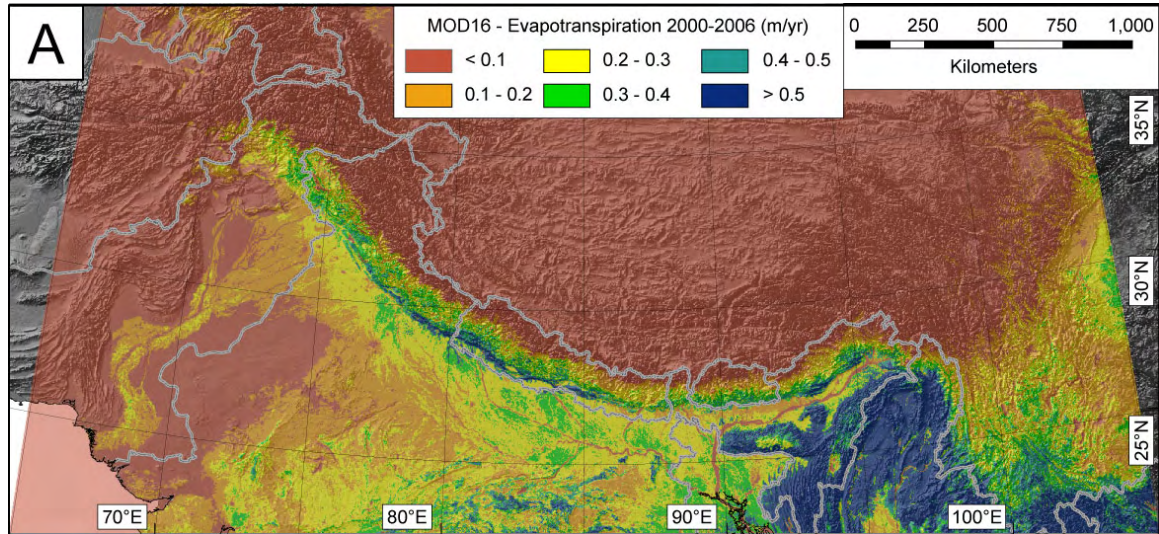

Figure DR5: Mean annual evapotranspiration (2000-2006) derived from the MODIS product MOD16 [Mu et al., 2007, Cleugh et al., 2007]. Note the high evapotranspiration amounts in the Himalayan foothills, the Ganges foreland, and the densely vegetated areas southeast of the Himalaya in the vicinity of the Shillong Plateau.

Results and Discussion

Based on our snowmelt model and the rainfall data, we calculated the fractional contribution made by snowmelt to the total discharge at any point in the catchment (see Figure 14). The map-based compilation reveals the importance of snowmelt throughout the year in the northwestern and northeastern Himalaya and at high elevations within the main Himalayan range (Figure DR6).
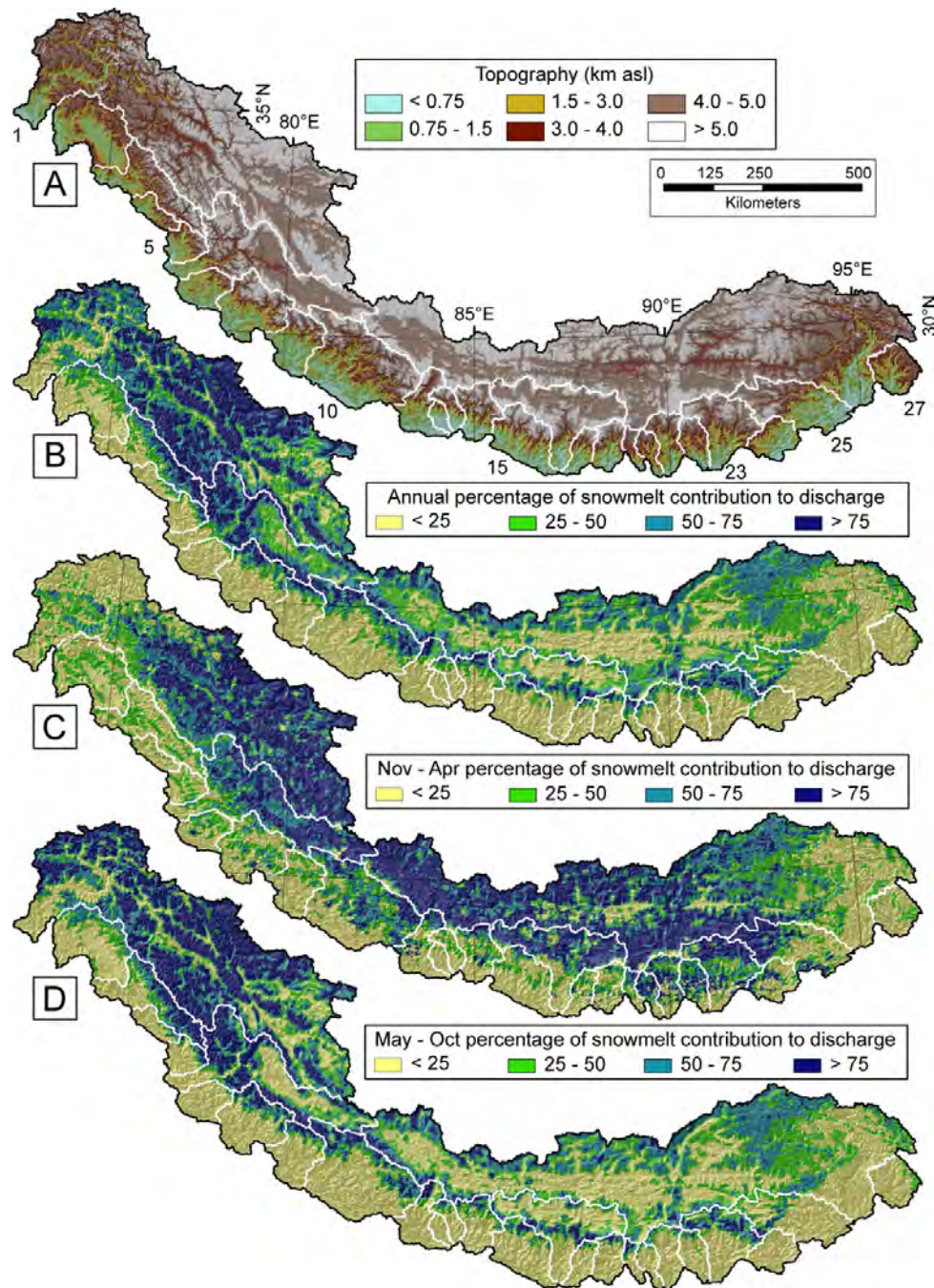
Figure DR 6: Overview and comparison of topography (A), annual (B) and seasonal (C-D) spatiotemporal discharge distribution derived from snowmelt. Note the high annual percentages (B) derived from snowmelt in the western catchments as well as in the high elevations along the Himalaya. The frontal areas are dominated by rainfall and thus have very low snowmelt contribution. During the winter (C), the southern parts of the Tibetan Plateau as well as high elevations area in all catchments contribute large amounts to river discharge. In the pre- and early-monsoon season (May to June), snowmelt from all catchments contributes significantly to river discharges (see also Figure 14 and 15).

In order to assess the quality of the snowmelt model and remotely sensed rainfall estimates, we compared our data to the gauged discharge from the Sutlej, Indus, and Titsa Rivers. Within the drier parts of the Sutlej catchment ($<3\text{x}10^{10}$ m^2), a linear log-log relationship exists of runoff versus area, irrespective of season (Figure DR7). Much higher rainfall south of the Himalayan crest (where catchment area exceeds $3\text{x}10^{10}$ m^2) drives abrupt increases in discharge and departure from the linear area-discharge relationship that exists upstream.
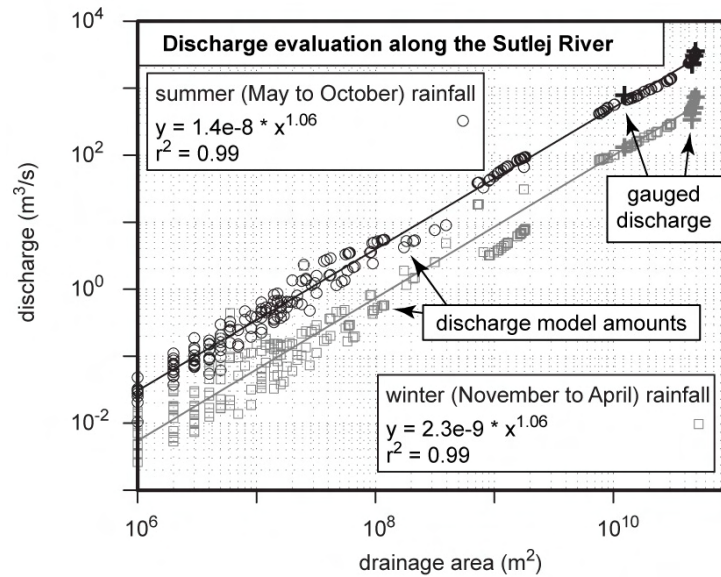

Figure DR7: Drainage area - discharge relation for the Sutlej River. Black circles show discharge during the summer, gray squares indicate winter discharge. Bold crosses are gauged discharge amounts. For both seasons, there is a robust power-law relation ($r^2 = 0.99$) between drainage area and discharge for most of the catchment. At drainage areas above $3\text{x}10^{10}$ m^2, discharge rapidly increases due to the influence of the monsoon.

Next, we analyze the relative rainfall and snowmelt contribution for the Sutlej River draining the southwestern Tibetan Plateau. During the summer time, discharge on the Tibetan Plateau side is dominated by rainfall contribution (~60%) and to a lesser degree by snowmelt contribution. This relation, however, changes downstream, when snowmelt from high-elevation ranges at the orographic barrier contributes more water to discharge. Only in the very downstream section near the southern end of the Himalaya, rainfall contribution becomes more important and reaches values above 50%.
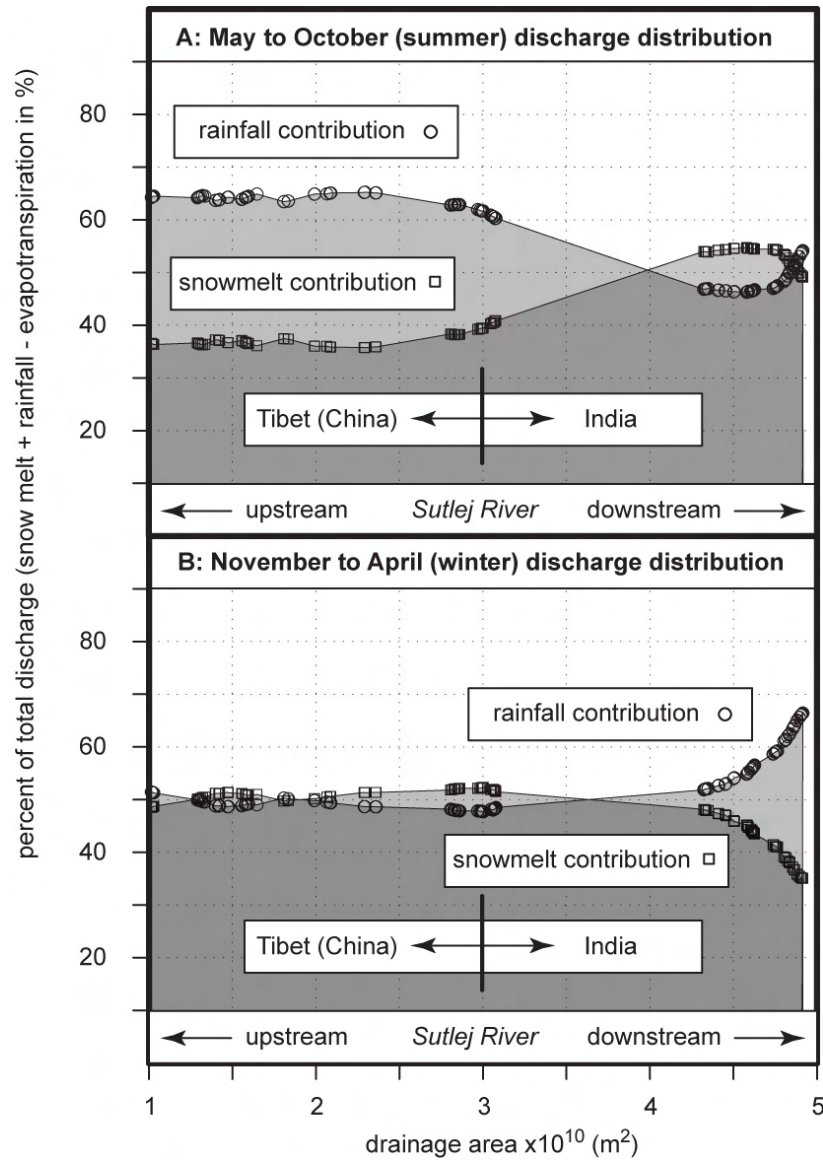
Figure DR8: Seasonal contribution of rainfall and snowmelt to total discharge for the Sutlej River. A shows summer and B winter season and focuses on drainage areas >10,000 km^2, encompassing the border region between China and India (see Figure 1 and DR1). During summer, rainfall dominates discharge amounts, except in the region of the orographic barrier (near 4.5×10^{10} m^2 in this figure), where high snow cover leads to a significant snowmelt contribution. During winter, discharge is dominated by rainfall only in the downstream, lower elevation areas. Note the large gaps between the points are due to drainage area increases when a tributary joins the Sutlej River.

References

Barros, A. P., and D. P. Lettenmaier (1994), Dynamic Modeling of Orographically Induced Precipitation, *Rev. Geophys.*, *32*(3), 265-284.

Bergeron, T. (1960), Operation and results of "Project Pluvius", in *Physics of Precipitation, Geophys. Monogr. Ser.*, edited by H. Weickmann, pp. 152-157, AGU, Washington, D.C.

Cleugh, H. A., et al. (2007), Regional evaporation estimates from flux tower and MODIS satellite data, *Remote Sensing of Environment*, *106*(3), 285-304.

Monteith, J. L. (1964), Evaporation and environment. The state and movement of water in living organisms, *Symposium of the society of experimental biology*, *Vol. 19*, 205-234, Cambridge: Cambridge University Press.

Mu, Q., et al. (2007), Development of a global evapotranspiration algorithm based on MODIS and global meteorology data, *Remote Sensing of Environment*, *111*(4), 519-536.

Roe, G. H. (2005), Orographic precipitation, *Annual Review of Earth and Planetary Sciences*, *33*, 645-671.

Smith, R. B. (1979), The influence of mountains on the atmosphere, *Advances in Geophysics*, *21*, 87-233.

Sun, Z. G., et al. (2007), Evaluation of MOD16 algorithm using MODIS and ground observational data in winter wheat field in North China Plain, *Hydrological Processes*, *21*(9), 1196-1206.